

**Keywords:** single-crystal X-ray diffraction; Laue method; Weissenberg method; rotation method; precession method; diffractometry.

## Single-crystal X-ray techniques

J. R. Helliwell\*

Department of Chemistry, University of Manchester, Manchester, M13 9PL, United Kingdom. \*Correspondence e-mail: john.helliwell@manchester.ac.uk

The diffraction of beams of X-rays from single crystals involves very specific geometries that form the basis for the measurement of intensities used in crystal structure analysis. In terms of the incident beam itself, the two key approaches available involve either a monochromatic beam or a polychromatic 'Laue' white beam. Starting from Bragg's law and the Ewald reciprocal-space construction, the methods for the collection of diffraction data, *i.e.* reflection intensities, using commonly available apparatus are then described. Monochromatic beam measuring methods such as rotating/oscillating crystal, stills, Weissenberg, precession and four-circle diffractometry are covered. The mathematical relationships between the reciprocal-lattice point (relp) coordinates in reciprocal space and the corresponding diffraction spot positions at the detector (flat, cylindrical or V-shaped) are given in detail. These coordinate transformations represent an idealized situation of relps (*i.e.* as points) and of diffracted rays as lines. Deviations from ideality arise from practical considerations such as the incident beam spectral purity, its divergence or convergence to the sample from the source *via* the optics, as well as the crystal perfection ('mosaicity'), and of the point-spread factor of the detector. The reflection rocking curves and diffraction spot shapes and sizes are practical manifestations of these effects.

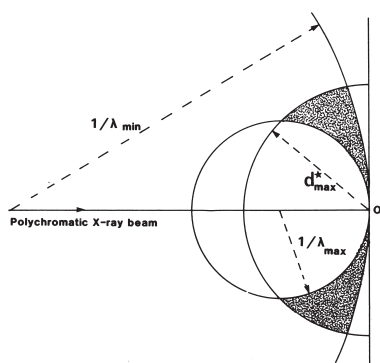
In the chapter *Classification of experimental techniques* (Helliwell, 2021) there are given the various common approaches to the recording of X-ray crystallographic data, in different geometries, for crystal structure analysis. These are:

- (a) Laue geometry;
- (b) monochromatic still exposure;
- (c) rotation/oscillation geometry;
- (d) Weissenberg geometry;
- (e) precession geometry; and
- (f) diffractometry.

The reasons for the choice of order are as follows. Laue geometry is dealt with first because it was historically the first to be used (Friedrich, Knipping & von Laue, 1912). Furthermore, in any case, the Laue method for quantitative structure analysis has enjoyed a revival at synchrotron radiation (SR) sources for time-resolved studies and is used extensively at neutron sources. The Laue method thus has a modern relevance. From consideration of the monochromatic still geometry, we can then describe the cases of single-axis rotation (rotation/oscillation method), single-axis rotation coupled with detector translation (Weissenberg method), crystal and detector precession (precession method), and finally three-axis goniostat and rotatable detector or area detector (diffractometry).

Where there are appropriate connections from the use of X-rays we make some specific references to use of neutrons or electrons.

Method (a) uses a polychromatic beam of broad wavelength bandpass (*e.g.*  $0.2 \leq \lambda \leq 2.5 \text{ \AA}$  with X-rays and to even longer



wavelengths, *e.g.* 5 Å, with neutrons, which are not heavily absorbed like X-rays at such wavelengths); if the bandwidth is restricted (*e.g.* to  $\delta\lambda/\lambda = 0.2$ ), then it is sometimes referred to as narrow-bandpass Laue geometry. The remaining methods (b)–(f) use a monochromatic beam.

There are textbooks that concentrate on almost every geometry. References to these books are given in the respective sections in the following pages. However, in addition, there are several books that contain extensive details of diffraction geometry. Blundell & Johnson (1976), Drenth (1994), Dauter & Wilson (2001) and Messerschmidt (2007) describe the use of the various diffraction geometries with the examples taken from protein crystallography. There is an extensive discussion and many practical details to be found in the textbooks of Stout & Jensen (1968), Woolfson (1970, 1997), Glusker & Trueblood (1971, 1985), Vainshtein (1981), McKie & McKie (1986), Aslanov *et al.* (1998) and Shmueli (2007), for example. A collection of early papers on the diffraction of X-rays by crystals involving, *inter alia*, experimental techniques and diffraction geometry, can be found in Bijvoet *et al.* (1969, 1972). A collection of papers on, primarily, protein and virus crystal data collection *via* the rotation-film method and diffractometry can be found in Wyckoff *et al.* (1985). Synchrotron instrumentation, methods and applications are dealt with in the books of Helliwell (1992) and Coppens (1992).

Quantitative X-ray crystal structure analysis usually involves methods (c), (d) and (f), although (e) has certainly been used. Electronic area detectors or image plates are extensively used now in all methods. Method (b), the use of monochromatic X-ray stills, is now growing in its usage with the advent of serial X-ray crystallography introduced at X-ray free-electron lasers (XFELs) and adopted also now at synchrotron X-ray sources [for a review see Patterson (2014)].

Traditionally, Laue photography has mostly been used for crystal orientation, crystal symmetry and mosaicity tests. Rapid recording of Laue patterns using synchrotron radiation, especially with protein crystals or with small crystals of small molecules, has led to a revival of interest in the use of Laue geometry for quantitative structure analysis. Various fundamental objections made, especially by W. L. Bragg, to the use of Laue geometry have been shown not to be limiting. Reactor neutron sources have also revived the Laue method for intensity measurements and it is also used at spallation neutron sources as a time-of-flight technique [see *e.g.* Forsyth *et al.* (1988), Langan *et al.* (2004), Schultz *et al.* (2005) and Tanaka *et al.* (2009)].

The monochromatic still photograph is typically used for orientation setting and mosaicity tests, for protein or virus crystallography, and computer refinement of crystal orientation following initial crystal setting. A ‘pink’ beam ( $\delta\lambda \simeq 0.02$  Å) is utilized for extracting more intensity from synchrotron X-ray or reactor neutron sources whilst preserving an essentially monochromatic still geometry. This type of incident beam is readily achieved using a multilayer beamline optical component.

Precession photography allows the isolation of a specific zone or plane of reflections for which indexing can be performed by inspection, and systematic absences and symmetry are explored. From this, space-group assignment is made. The use of precession photography is usually avoided these days where auto-indexing methods are employed on a single-crystal diffractometer. Inspection of zones of intensity is still made available as a useful diagnostic on modern diffractometers using the rotation method. The precession method (without a layer-line screen) is enjoying a revival in measurements made in electron crystallography (Vincent & Midgley, 1994).

In the following sections, the geometry of each method is dealt with in an idealized form. The practical realization of each geometry is then dealt with, including any geometric distortions introduced in the image by electronic area detectors. A separate section deals with the common means for beam conditioning, namely mirrors, monochromators and filters. Sufficient detail is given to establish the magnitude of the wavelength range, spectral spreads, beam divergence and convergence angles, and detector effects. These values can then be utilized along with the formulae given for the calculation of spot bandwidth, spot size and angular reflecting range.

In each of these diffraction geometries the diffuse scattering features between and underneath the Bragg peaks may be discerned, depending on the sample, but specific steps are taken for the measuring and the extraction of the diffuse scattering intensities. For the pair distribution function (PDF) method reference can be made to Billinge (2019). For a wide-ranging review of diffuse scattering including a historical summary for the last 100 years, including experimental measurement protocols, see Welberry & Weber (2016). Specific experimental details for measuring diffuse scattering from crystals of biological macromolecules can be found for example in Chapter 2.1 of Wall (1996) and in Glover *et al.* (1991).

### 1. Laue geometry

The main book dealing with Laue geometry is Amorós *et al.* (1975). This can usefully be used in conjunction with Henry *et al.* (1951), or McKie & McKie (1986); see also Chapter 7 of Helliwell (1992), Chapter 8 of Messerschmidt (2007) and Chapter 4 of Shmueli (2007). There is a synergy between synchrotron and reactor neutron Laue diffraction developments (see Helliwell & Wilkinson, 1994).

I mention here that the discussion below focuses on the use of flat-plate geometry, but where exceptions are used today then these are mentioned explicitly and a reference is given.

#### 1.1. General

The single crystal is bathed in a polychromatic beam of X-rays containing wavelengths between  $\lambda_{\min}$  and  $\lambda_{\max}$ . A particular crystal plane will pick out a general wavelength  $\lambda$

for which constructive interference occurs and reflect according to Bragg's law

$$\lambda = 2d \sin \theta, \quad (1)$$

where  $d$  is the interplanar spacing and  $\theta$  is the angle of reflection. A sphere drawn with radius  $1/\lambda$  and with the beam direction as diameter, passing through the origin of the reciprocal lattice (the point  $O$  in Fig. 1), will yield a reflection in the direction drawn from the centre of the sphere and out through the reciprocal-lattice point (relp) provided the relp in question lies on the surface of the sphere. This sphere is known as the Ewald sphere. Fig. 1 shows the Laue geometry, in which there exists a nest of Ewald spheres of radii between  $1/\lambda_{\max}$  and  $1/\lambda_{\min}$ . An alternative convention is feasible whereby only a single Ewald sphere is drawn of radius  $1$  reciprocal-lattice unit (r.l.u.). Then each relp is no longer a point but a streak between  $\lambda_{\min}/d$  and  $\lambda_{\max}/d$  from the origin of reciprocal space (see McKie & McKie, 1986, p. 297). In the following discussions on the Laue approach, this notation is not followed. We use the nest of Ewald spheres of varying radii instead.

Any relp ( $hkl$ ) lying in the region of reciprocal space between the  $1/\lambda_{\max}$  and  $1/\lambda_{\min}$  Ewald spheres and the reso-

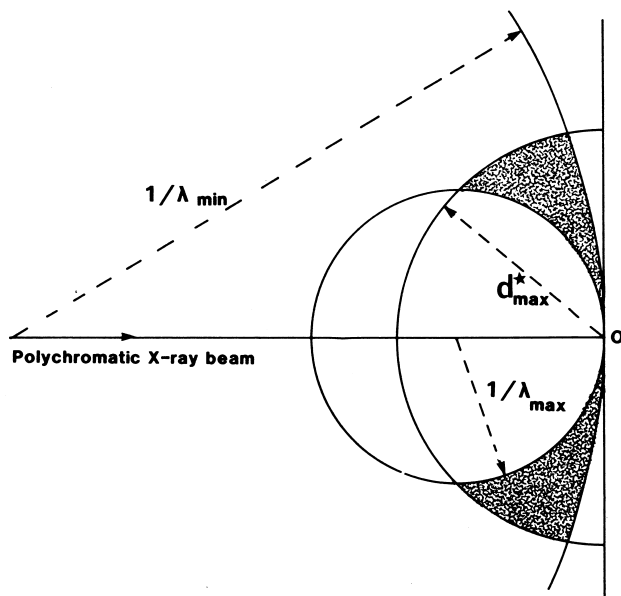


**Figure 1**

Laue geometry. A polychromatic beam containing wavelengths  $\lambda_{\min}$  to  $\lambda_{\max}$  impinges on the crystal sample. The resolution sphere of radius  $\lambda_{\max}^* = 1/d_{\min}$  is drawn centred at  $O$ , the origin of reciprocal space. Any reciprocal-lattice point falling in the shaded region is stimulated. In this diagram, the radius of each Ewald sphere uses the convention  $1/\lambda$ . Note the restriction on the resolution limit occurring because of the flat plate, whereas with a cylindrical geometry one can record diffraction data for larger  $2\theta$  angles and increase the resolution limit. The cylindrical neutron sensitive image plate is actively used today for macromolecular neutron crystallography diffraction data collection at reactor neutron sources (see Blakeley, 2009) where a LAue Diffractometer ('LADI') instrument reaches  $2\theta$  measurements of  $180^\circ$ . Historically such a 'wrap around' cylindrical geometry was the basis of both the original 'Bernal rotation camera' and the original 'Weissenberg camera' used in the past with photographic film for X-ray diffraction measurements from small-molecule organic and inorganic crystals.

lution sphere  $1/d_{\min}$  will diffract (the shaded area in Fig. 1). This region of reciprocal space is referred to as the accessible or stimulated region. Fig. 2 shows a predicted Laue pattern from a well aligned protein crystal. For a description of the indexing of a Laue photograph, see Bragg (1928, pp. 28, 29).

For a Laue spot at a given  $\theta$ , only the ratio  $\lambda/d$  is determined, and whether it is a single or a multiple relp component spot. If the unit-cell parameters are known from a monochromatic experiment, then a Laue spot at a given  $\theta$  yields  $\lambda$  since  $d$  is then known. Conversely, precise unit-cell lengths cannot be determined from a Laue pattern alone; methods are, however, available to help determine these (see Carr *et al.*, 1992).

The maximum Bragg angle  $\theta_{\max}$  is given by the equation

$$\theta_{\max} = \sin^{-1}(\lambda_{\max}/2d_{\min}). \quad (2)$$

## 1.2. Crystal setting

The main use of Laue photography has in the past been for adjustment of the crystal to a desired orientation. With small-molecule crystals, the number of diffraction spots on a monochromatic photograph from a stationary crystal is very small. With unfiltered, polychromatic radiation, many more spots are observed and so the Laue photograph can give a clear indication of the crystal orientation and setting. Currently, with small-molecule or protein crystals for structure determination, the monochromatic still or small-angular-range rotation diffraction image is used for this purpose before data collection *via* an area detector. Synchrotron-radiation Laue photographs of protein crystals can be recorded with ultra-short exposure times such as into the sub-nanosecond range (Moffat, 2001). For a review see Ren *et al.* (1999). These patterns consist of a large number of diffraction spots. There has been a trend to narrower wavelength bandpasses to optimize intensity signal to noise and this leads to fewer diffraction spots. This can lead to auto-indexing difficulties in determining the crystal setting.

Crystal setting *via* Laue photography usually involves trying to direct the X-ray beam along a zone axis. Angular mis-setting angles  $\varepsilon$  in the spindle and arc are easily calculated from the formula

$$\varepsilon = \tan^{-1}(\Delta/D), \quad (3)$$

where  $\Delta$  is the distance (resolved into vertical and horizontal) from the beam centre to the centre of a circle of spots defining a zone axis and  $D$  is the crystal-to-film distance.

After suitable angular correction to the sample orientation, the Laue photograph will show a pronounced blank region at the centre of the film (see Fig. 2). This radius of the blank region is determined by the minimum wavelength in the beam and the magnitude of the reciprocal-lattice spacing parallel to the X-ray beam (see Jeffery, 1958). For the case, for example, of the X-ray beam perpendicular to the  $a^*b^*$  plane, then

$$\lambda_{\min} = c(1 - \cos 2\theta), \quad (4a)$$

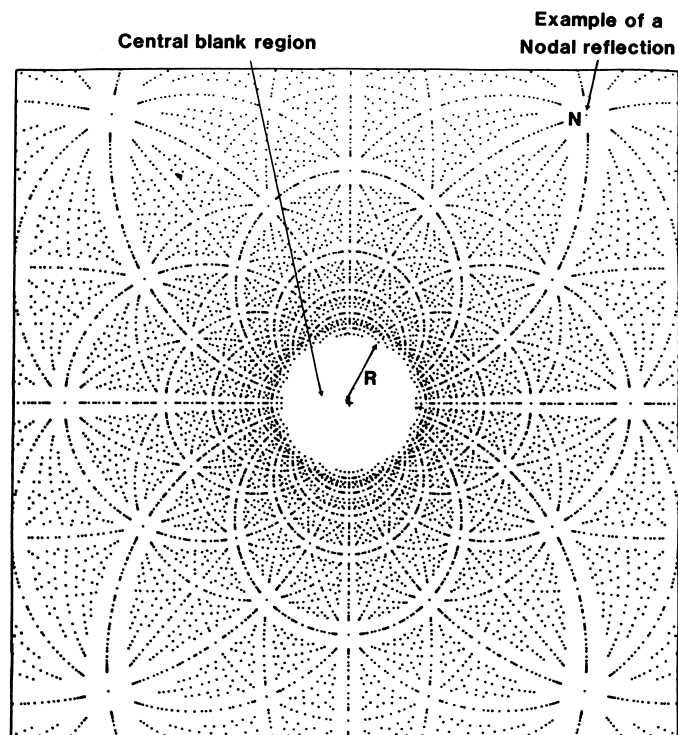


**Figure 2**  
A predicted Laue pattern of a protein crystal with a zone axis parallel to the incident, polychromatic X-ray beam. There is a pronounced blank region at the centre of the film (see Section 1.2). The spot marked *N* is one example of a nodal spot (see Section 1.4).

where

$$2\theta = \tan^{-1}(R/D), \tag{4b}$$

where *R* is the radius of the blank region (see Fig. 2) and *D* is the crystal-to-flat-film distance. If  $\lambda_{\min}$  is known then an approximate value of *c*, for example, can be estimated. The principal zone axes will give the largest radii for the central blank region.

The treatment above is for when the incident X-ray beam is able to pass through the sample, *i.e.* in what is referred to as transmission Laue diffraction. For the cases of huge crystals of inorganic/small-molecule materials transmission of the X-ray beam does not occur and crystal setting is then made in a ‘back-reflection’ mode of measurement. This is used by crystal growers targetting industrial applications of such large crystals. See *e.g.* Amorós *et al.* (1975), pp. 103–105.

### 1.3. Single-order and multiple-order reflections

In Laue geometry, several relp’s can occur in a Laue spot or ray. The number of relp’s in a given spot is called the multiplicity of the spot. The number of spots of a given multiplicity can be plotted as a histogram. This is known as the multiplicity distribution. The form of this distribution is dependent on the ratio  $\lambda_{\max}/\lambda_{\min}$ . The multiplicity distribution in Laue diffraction is considered in detail by Cruickshank *et al.* (1987).

Any relp *nh, nk, nl* (*n* integer) will be stimulated by a wavelength  $\lambda/n$  since  $d_{nhnknl} = d_{hkl}/n$ , *i.e.*

$$\frac{\lambda}{n} = 2 \frac{d_{hkl}}{n} \sin \theta. \tag{5}$$

However,  $d_{nhnknl}$  must be within the sample resolution limit.

If *h, k, l* have no common integer divisor and if *2h, 2k, 2l* is beyond the resolution limit, then the spot on the Laue diffraction photograph is a single-wavelength spot. The probability that *h, k, l* have no common integer divisor is

$$Q = \left[1 - \frac{1}{2^3}\right] \left[1 - \frac{1}{3^3}\right] \left[1 - \frac{1}{5^3}\right] \dots = 0.832 \dots \tag{6}$$

Hence, for a relp where  $d_{\min} < d_{hkl} < 2d_{\min}$  there is a very high probability (83.2%) that the Laue spot will be recorded as a single-wavelength spot. Since this region of reciprocal space corresponds to 87.5% (*i.e.* 7/8) of the volume of reciprocal space within the resolution sphere then  $0.875 \times 0.832 = 72.8\%$  is the probability for a relp to be recorded in a single-wavelength spot. According to W. L. Bragg, all Laue spots should be multiple. He reasoned that for each *h, k, l* there will always be a *2h, 2k, 2l* *etc.* lying within the same Laue spot. However, as the resolution limit is increased to accommodate this many more relp’s are added, for which their *hkl*’s have no common integer divisor.

The above discussion holds for infinite bandwidth. The effect of a more experimentally realistic bandwidth is to increase the proportion of single-wavelength spots.

The number of relp’s within the resolution sphere is

$$\frac{4}{3} \frac{\pi d_{\max}^{*3}}{V^*}, \tag{7}$$

where  $d_{\max}^* = 1/d_{\min}$  and  $V^*$  is the reciprocal unit-cell volume.

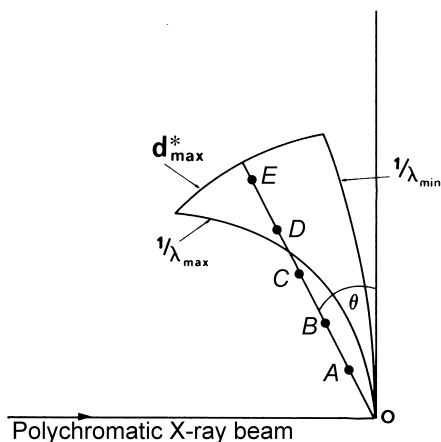


Figure 3

A multiple component spot in Laue geometry. A ray of multiplicity 5 is shown as an example. The inner point *A* corresponds to *d* and a wavelength  $\lambda$ , the next point, *B*, is  $d/2$  and wavelength  $\lambda/2$ . The outer point *E* corresponds to  $d/5$  and  $\lambda/5$ . Rotation of the sample will either exclude inner points (at the  $\lambda_{\max}$  surface) or outer points (at the  $\lambda_{\min}$  surface) and so determine the recorded multiplicity.

The number of relp's within the wavelength band  $\lambda_{\max}$  to  $\lambda_{\min}$ , for  $\lambda_{\max} < 2/d_{\max}^*$ , is (Moffat *et al.*, 1986)

$$\frac{\pi}{4} \frac{(\lambda_{\max} - \lambda_{\min}) d_{\max}^{*4}}{V^*} \quad (8)$$

Note that the number of relp's stimulated in a 0.1 Å wavelength interval, for example between 0.1 and 0.2 Å, is the same as that between 1.1 and 1.2 Å, for example. A large number of relp's are stimulated at one orientation of the crystal sample.

The proportion of relp's within a sphere of small  $d^*$  (*i.e.* at low resolution) actually stimulated is small. In addition, the

probability of them being single is zero in the infinite-bandwidth case and small in the finite-bandwidth case. However, Laue geometry is an efficient way of measuring a large number of relp's between  $d_{\max}^*$  and  $d_{\max}^*/2$  as single-wavelength spots. In any case multiplet spots are now readily deconvoluted to their single component intensities where there are enough observations *e.g.* from various crystal orientations (see Nieh *et al.*, 1999, and Ren *et al.*, 1999).

The above is a brief description of the overall multiplicity distribution. For a given relp, even of simple *hkl* values, lying on a ray of several relp's (multiples of *hkl*), a suitable choice of crystal orientation can yield a single-wavelength spot. Consider, for example, a spot of multiplicity 5. The outermost relp can be recorded at long wavelength with the inner relp's on the ray excluded since they need  $\lambda$ 's greater than  $\lambda_{\max}$  (Fig. 3). Alternatively, by rotating the sample, the innermost relp can be measured uniquely at short wavelength with the outer relp's excluded (they require  $\lambda$ 's shorter than  $\lambda_{\min}$ ). The multiplicity distribution is shown in Fig. 4 as a function of  $\lambda_{\max}/\lambda_{\min}$  (with the corresponding values of  $\delta\lambda/\lambda_{\text{mean}}$ ).

#### 1.4. Angular distribution of reflections in Laue diffraction

There is an interesting variation in the angular separations of Laue reflections that shows up in the spatial distributions of spots on a detector plane (Cruickshank *et al.*, 1991). There are two main aspects to this distribution, which are general and local. The general aspects refer to the diffraction pattern as a whole and the local aspects to reflections in a particular zone of diffraction spots.

The general features include the following. The spatial density of spots is everywhere proportional to  $1/D^2$ , where *D* is

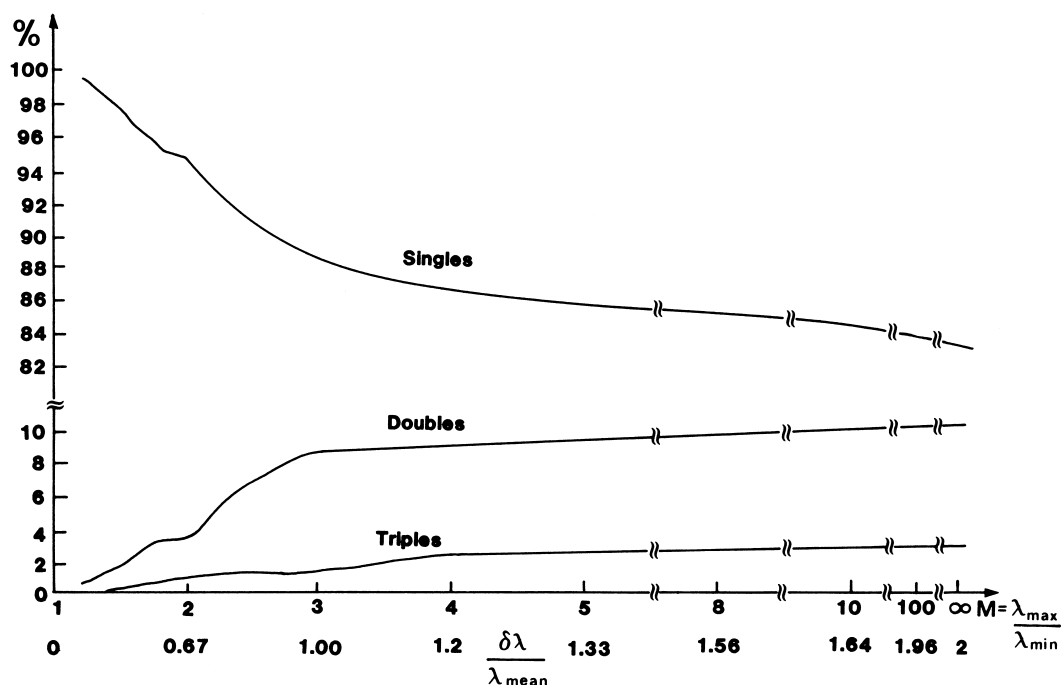


Figure 4

The variation with  $M = \lambda_{\max}/\lambda_{\min}$  of the proportions of relp's lying on single, double and triple rays for the case  $\lambda_{\max} < 2/d_{\max}^*$ . From Cruickshank *et al.* (1987).

the crystal-to-detector distance, and to  $1/V^*$ , where  $V^*$  is the reciprocal-cell volume. There is also though a substantial variation in spatial density with diffraction angle  $\theta$ ; a prominent maximum occurs at

$$\theta_c = \sin^{-1}(\lambda_{\min} d_{\max}^*/2). \tag{9}$$

Local aspects of these patterns particularly include the prominent conics on which Laue reflections lie. That is, the local spatial distribution is inherently one-dimensional in character. Between multiple reflections (nodals), there is always at least one single and therefore nodals have a larger angular separation from their nearest neighbours. The blank area around a nodal in a Laue pattern (Fig. 2) has been noted by Jeffery (1958). The smallest angular separations, and therefore spatially overlapped cases, are associated with single Laue reflections. Thus, the reflections involved in energy overlaps – the multiples – form a set largely distinct, except at short crystal-to-detector distances, from those involved in spatial overlaps, which are mostly singles (Helliwell, 1985).

From a knowledge of the form of the angular distribution, it is possible, e.g. from the gaps bordering conics, to estimate  $d_{\max}^*$  and  $\lambda_{\min}$ . A development of this involving gnomonic projections can be even more effective (Cruickshank *et al.*, 1992).

### 1.5. Gnomonic and stereographic transformations

A useful means of transformation of the flat-detector Laue pattern is the gnomonic projection. This converts the pattern of spots lying on curved arcs to points lying on straight lines. The stereographic projection is also used. Fig. 5 shows the graphical relationships involved [taken from *International Tables for X-ray Crystallography*, Vol. II (Evans & Lonsdale, 1959)], for the case of a Laue pattern recorded on a plane film, between the incident-beam direction  $SN$ , which is perpendicular to the film plane, and the Laue spot  $L$ , and its spherical,

stereographic and gnomonic points  $S_p$ ,  $S_t$  and  $G$  and the stereographic projection  $S_r$  of the reflected beams. If the radius of the sphere of projection is taken equal to  $D$ , the crystal-to-film distance, then the planes of the gnomonic projection and of the film coincide. The lines producing the various projection poles for any given crystal plane are coplanar with the incident and reflected beams. The transformation equations are

$$P_L = D \tan 2\theta \tag{10}$$

$$P_G = D \cot \theta \tag{11}$$

$$P_S = D \frac{\cos \theta}{(1 + \sin \theta)} \tag{12}$$

$$P_R = D \tan \theta. \tag{13}$$

## 2. Monochromatic methods

In this section and those that follow, which deal with monochromatic methods, the convention is adopted that the Ewald sphere takes a radius of unity and the magnitude of the reciprocal-lattice vector is  $\lambda/d$ . This is not the convention used in the Laue section above.

Some historical remarks are useful first before progressing to discuss each monochromatic geometry in detail. The original rotation method (for example, see Bragg, 1949) involved a rotation of a perfectly aligned crystal through  $360^\circ$ . For reasons of relatively poor collimation of the X-ray beam, leading to spot-to-spot overlap, and background build-up, Bernal (1927) introduced the oscillation method whereby a repeated, limited, angular range was used to record one pattern and a whole series of contiguous ranges on different film exposures were collected to provide a large angular coverage overall. In a different solution to the same problem, Weissenberg (1924) utilized a layer-line screen to record only one layer line but allowed a full rotation of the crystal but now coupled to translation of the detector, thus avoiding spot-to-spot overlap. Again, several exposures were needed, involving one layer line collected on each exposure. The advent of synchrotron radiation with very high intensity allows small beam sizes at the sample to be practicable, thus simultaneously creating small diffraction spots and minimizing background scatter. The very fine collimation of the synchrotron beam keeps the diffraction-spot sizes as small as possible as they traverse their path to the detector plane (see Section 7.3), whichever diffractometer or camera setup is used.

The terminology used today for different methods is essentially the same as originally used except that the rotation method now tends to mean limited angular ranges (instead of  $360^\circ$ ) per diffraction photograph/image. The Weissenberg method in its modern form as has been employed at a synchrotron is a screenless technique with limited angular range but still with detector translation coupled to crystal rotation.

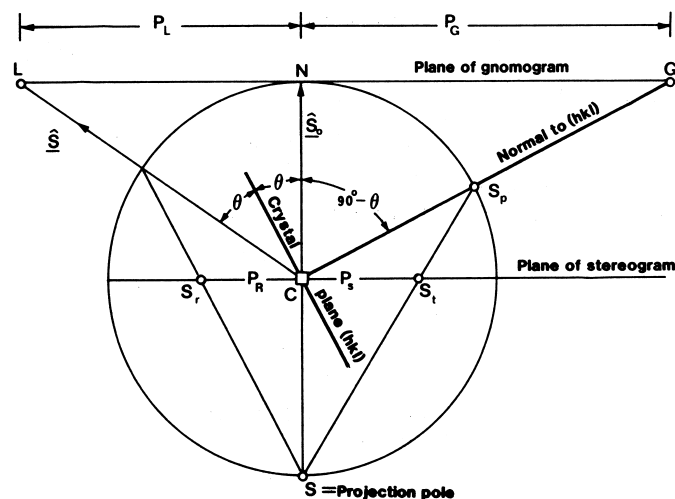


Figure 5 Geometrical principles of the spherical, stereographic, gnomonic and Laue projections. From Evans & Lonsdale (1959).

## 2.1. Monochromatic still exposure

In a monochromatic still exposure, the crystal is held stationary and a near-zero wavelength bandpass (*e.g.*  $\delta\lambda/\lambda = 0.001$ ) beam impinges on it. For a small-molecule crystal, there are few diffraction spots. For a protein crystal, there are many (several hundred), because of the much denser reciprocal lattice. The actual number of stimulated reflections depends on the reciprocal-cell parameters, the size of the mosaic spread of the crystal, the angular beam divergence as well as the small, but finite, spectral spread,  $\delta\lambda/\lambda$ . Diffraction spots are only partially stimulated instead of fully integrated over wavelength, as in the Laue method, or over an angular rotation (the rocking width) in rotating-crystal monochromatic methods.

The diffraction spots lie on curved arcs where each curve corresponds to the intersection of a cone with a film (or detector). With a flat film the intersections are conic sections.

The curved arcs are most obviously recognizable for the protein crystal case where there are a large number of spots.

## 2.2. Crystal setting

Crystal setting follows the procedure given in Section 1.2 whereby angular mis-setting angles are given by equation (3). When viewed down a zone axis, the pattern on the detector has the appearance of a series of concentric circles. For example, with the beam parallel to  $[00\bar{1}]$ , the first circle corresponds to  $l = 1$ , the second to  $l = 2$ , *etc.* The radius of the first circle  $R$  is related to the interplanar spacing between the  $(hk0)$  and  $(hk1)$  planes, *i.e.*  $\lambda/c$  (in this example), through  $\theta$ , by the formulae

$$\tan 2\theta = R/D; \quad \cos 2\theta = 1 - \lambda/c. \quad (14)$$

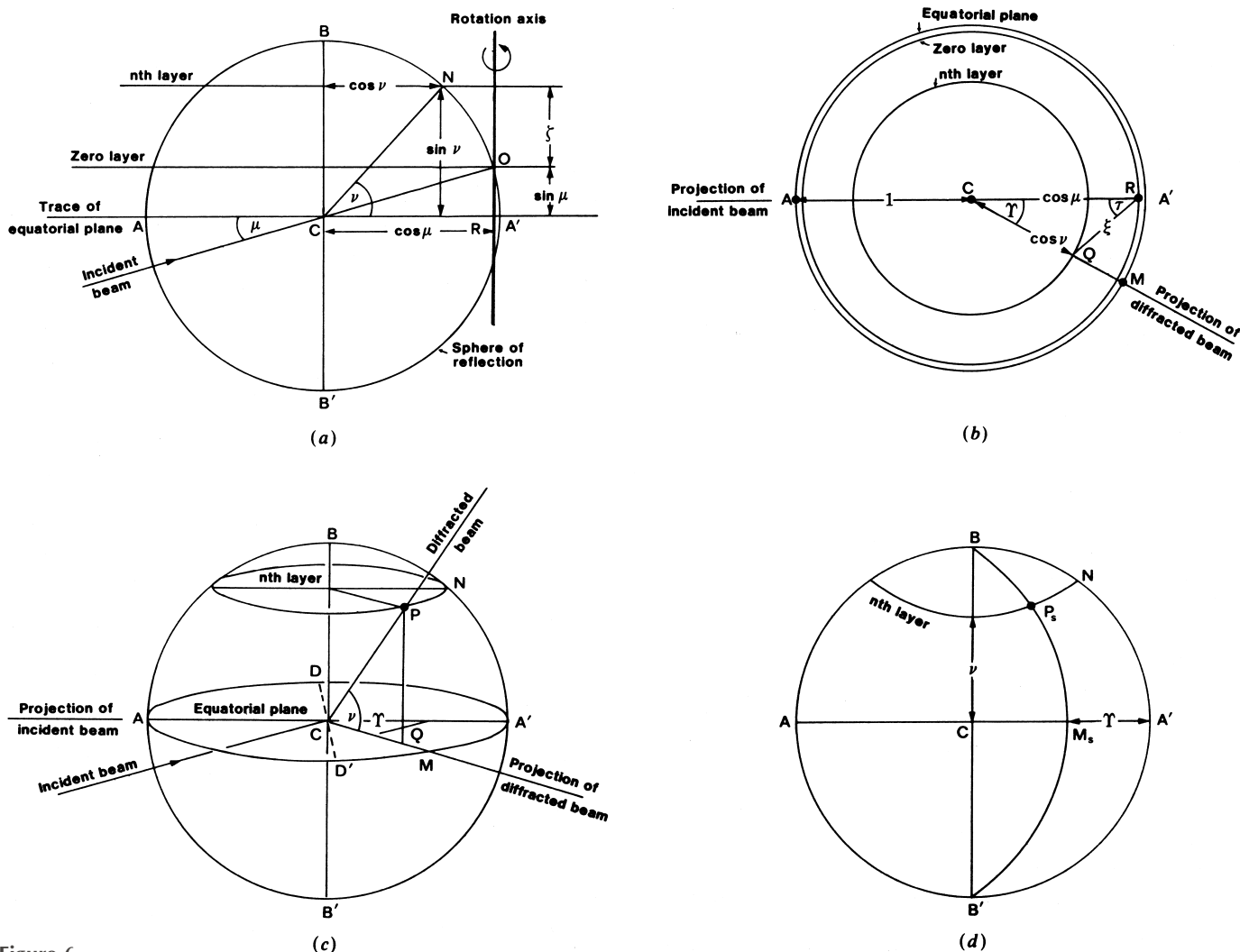


Figure 6

(a) Elevation of the sphere of reflection.  $O$  is the origin of the reciprocal lattice.  $C$  is the centre of the Ewald sphere. The incident beam is shown in the plane. (b) Plan of the sphere of reflection.  $R$  is the projection of the rotation axis on the equatorial plane. (c) Perspective diagram.  $P$  is the reflection in the reflection position with the cylindrical coordinates  $\zeta, \xi, \varphi$ . The angular coordinates of the diffracted beam are  $\nu, \Upsilon$ . (d) Stereogram to show the direction of the diffracted beam,  $\nu, \Upsilon$ , with  $DD'$ , normal to the incident beam and in the equatorial plane, as the projection diameter. From Evans & Lonsdale (1959).

**Table 1**

Glossary of symbols used to specify quantities on diffraction patterns and in reciprocal space.

The equatorial plane is the plane normal to the rotation axis.

$\theta$	Bragg angle
$2\theta$	Angle of deviation of the reflected beam with respect to the incident beam
$\hat{S}_o$	Unit vector lying along the direction of the incident beam
$\hat{S}$	Unit vector lying along the direction of the reflected beam
$s = (\hat{S} - \hat{S}_o)$	The scattering vector of magnitude $2 \sin \theta$ . $s$ is perpendicular to the bisector of the angle between $\hat{S}_o$ and $\hat{S}$ . $s$ is identical to the reciprocal-lattice vector $\mathbf{d}^*$ of magnitude $\lambda/d$ , where $d$ is the interplanar spacing, when $\mathbf{d}^*$ is in the diffraction condition. In this notation, the radius of the Ewald sphere is unity. This convention is adopted because it follows that in Volume II of <i>International Tables for X-ray Crystallography</i> (p. 175). Note that in Section 1 <i>Laue geometry</i> the alternative convention ( $ \mathbf{d}^*  = 1/d$ ) is adopted whereby the radius of each Ewald sphere is $1/\lambda$ . This allows a nest of Ewald spheres between $1/\lambda_{\max}$ and $1/\lambda_{\min}$ to be drawn
$\zeta$	Coordinate of a point $P$ in reciprocal space parallel to a rotation axis as the axis of cylindrical coordinates relative to the origin of reciprocal space
$\xi$	Radial coordinate of a point $P$ in reciprocal space; that is, the radius of a cylinder having the rotation axis as axis
$\tau$	The angular coordinate of $P$ , measured as the angle between $\xi$ and $\hat{S}_o$ [see Fig. 6(b)]
$\varphi$	The angle of rotation from a defined datum orientation to bring a reflp onto the Ewald sphere in the rotation method (see Fig. 8)
$\mu$	The angle of inclination of $\hat{S}_o$ to the equatorial plane
$\Upsilon$	The angle between the projections of $\hat{S}_o$ and $\hat{S}$ onto the equatorial plane
$\nu$	The angle of inclination of $\hat{S}$ to the equatorial plane
$\omega, \chi, \varphi$	The crystal setting angles on the four-circle diffractometer (see Fig. 11). The $\varphi$ used here is not the same as that in the rotation method (Fig. 8). This clash in using the same symbol twice is inevitable because of the widespread use of the rotation camera and four-circle diffractometer

### 3. Rotation/oscillation geometry

The main book dealing with the rotation method is that of Arndt & Wonacott (1977).

#### 3.1. General

The purpose of the monochromatic rotation method is to stimulate a reflection fully over its rocking width *via* an angular rotation. Different reflp's are rotated successively into the reflecting position. The method, therefore, involves rotation of the sample about a single axis, and is used in conjunction with an area detector of some sort, *e.g.* a charge-coupled device (CCD) or pixel area detector or image plate. The use of a repeated rotation or oscillation, for a given exposure, is simply to average out any time-dependent changes in incident intensity or sample decay. The overall crystal rotation required to record the total accessible region of reciprocal space for a single crystal setting, and a detector picking up all the diffraction spots, is  $180^\circ + 2\theta_{\max}$ . If the crystal has additional symmetry, then a complete asymmetric unit of reciprocal space can be recorded within a smaller angle. There is a blind region close to the rotation axis; this is detailed in Section 3.5.

#### 3.2. Diffraction coordinates

Fig. 6(a) to (d) are taken from *International Tables for X-ray Crystallography* Vol. II (1959, p. 176). They neatly summarize the geometrical principles of reflection of a monochromatic beam, in the reciprocal lattice, for the general case of an incident beam inclined at an angle ( $\mu$ ) to the equatorial plane. The diagrams are based on an Ewald sphere of unit radius.

With the nomenclature of Table 1:

Fig. 6(a) gives

$$\sin \nu = \sin \mu + \zeta. \tag{15}$$

Fig. 6(b) gives, by the cosine rule,

$$\cos \Upsilon = \frac{\cos^2 \nu + \cos^2 \mu - \xi^2}{2 \cos \nu \cos \mu} \tag{16}$$

and

$$\cos \tau = \frac{\cos^2 \mu + \xi^2 - \cos^2 \nu}{2 \xi \cos \mu}, \tag{17}$$

and Fig. 6(a) and (b) give

$$\xi^2 + \zeta^2 = d^{*2} = 4 \sin^2 \theta. \tag{18}$$

The following special cases commonly occur:

(a)  $\mu = 0$ , normal-beam rotation method, then

$$\sin \nu = \zeta \tag{19}$$

and

$$\cos \Upsilon = \frac{2 - \xi^2 - \zeta^2}{2(1 - \zeta^2)^{1/2}}; \tag{20}$$

(b)  $\mu = -\nu$ , equi-inclination (relevant to Weissenberg upper-layer photography), then

$$\zeta = -2 \sin \mu = 2 \sin \nu \tag{21}$$

$$\cos \Upsilon = 1 - \frac{\xi^2}{2 \cos^2 \nu}; \tag{22}$$

(c)  $\mu = +\nu$ , anti-equi-inclination

$$\zeta = 0 \tag{23}$$

$$\cos \Upsilon = 1 - \frac{\xi^2}{2 \cos^2 \nu}; \tag{24}$$

(d)  $\nu = 0$ , flat cone

$$\zeta = -\sin \mu \tag{25}$$

$$\cos \Upsilon = \frac{2 - \xi^2 - \zeta^2}{2(1 - \zeta^2)^{1/2}}. \quad (26)$$

In this section, we will concentrate on case (a), the normal-beam rotation method ( $\mu = 0$ ). First, the case of a plane film or detector is considered.

The notation now follows that of Arndt & Wonacott (1977) for the coordinates of a spot on the film or detector.  $Z_F$  is parallel to the rotation axis and  $\zeta$ .  $Y_F$  is perpendicular to the rotation axis and the beam. *International Tables for X-ray*

*Crystallography* Vol. II (1959, p. 177) follows the convention of  $y$  being parallel and  $x$  perpendicular to the rotation-axis direction, *i.e.*  $(Y_F, Z_F) \equiv (x, y)$ . The advantage of the  $(Y_F, Z_F)$  notation is that the  $x$ -axis direction is then the same as the X-ray beam direction.

The coordinates of a reflection on a flat film ( $Y_F, Z_F$ ) are related to the cylindrical coordinates of a reflp ( $\xi, \zeta$ ) [Fig. 7(a)] by

$$Y_F = D \tan \Upsilon \quad (27)$$

$$Z_F = D \sec \Upsilon \tan \nu, \quad (28)$$

which becomes

$$Z_F = 2D\zeta/(2 - \xi^2 - \zeta^2), \quad (29)$$

where  $D$  is the crystal-to-film distance.

For the case of a V-shaped cassette with the V axis parallel to the rotation axis and the film making an angle  $\alpha$  to the beam direction [Fig. 7(b)], then

$$Y_F = D \tan \Upsilon / (\sin \alpha + \cos \alpha \tan \Upsilon) \quad (30)$$

$$Z_F = (D - Y_F \cos \alpha) \zeta / (1 - d^{*2}/2). \quad (31)$$

This situation also corresponds to the case of a flat electronic area detector inclined to the incident beam in a similar way.

Note that Arndt & Wonacott (1977) use  $\nu$  instead of  $\alpha$  here. We use  $\alpha$  and so follow *International Tables for X-ray Crystallography* Vol. II (1959). This avoids confusion with the  $\nu$  of Table 1.  $D$  is the crystal to V distance. In the case of the V cassettes of Enraf–Nonius,  $\alpha$  is  $60^\circ$ .

For the case of a cylindrical film or image plate where the axis of the cylinder is coincident with the rotation axis [Fig. 7(c)] then, for  $\Upsilon$  in degrees,

$$Y_F = \frac{2\pi}{360} D \Upsilon \quad (32)$$

$$Z_F = D \tan \nu, \quad (33)$$

which becomes

$$Z_F = \frac{D\zeta}{(1 - \zeta^2)^{1/2}}. \quad (34)$$

Here,  $D$  is the radius of curvature of the cylinder assuming that the crystal is at the centre of curvature.

In the three geometries mentioned here, detector-misalignment errors have to be considered. These are three orthogonal angular errors, translation of the origin, and error in the crystal-to-film distance.

The coordinates  $Y_F$  and  $Z_F$  are related to film-scanner raster units *via* a scanner-rotation matrix and translation vector. This is necessary because the film is placed arbitrarily on the scanner drum. Details can be found in Rossmann (1985) or Arndt & Wonacott (1977).

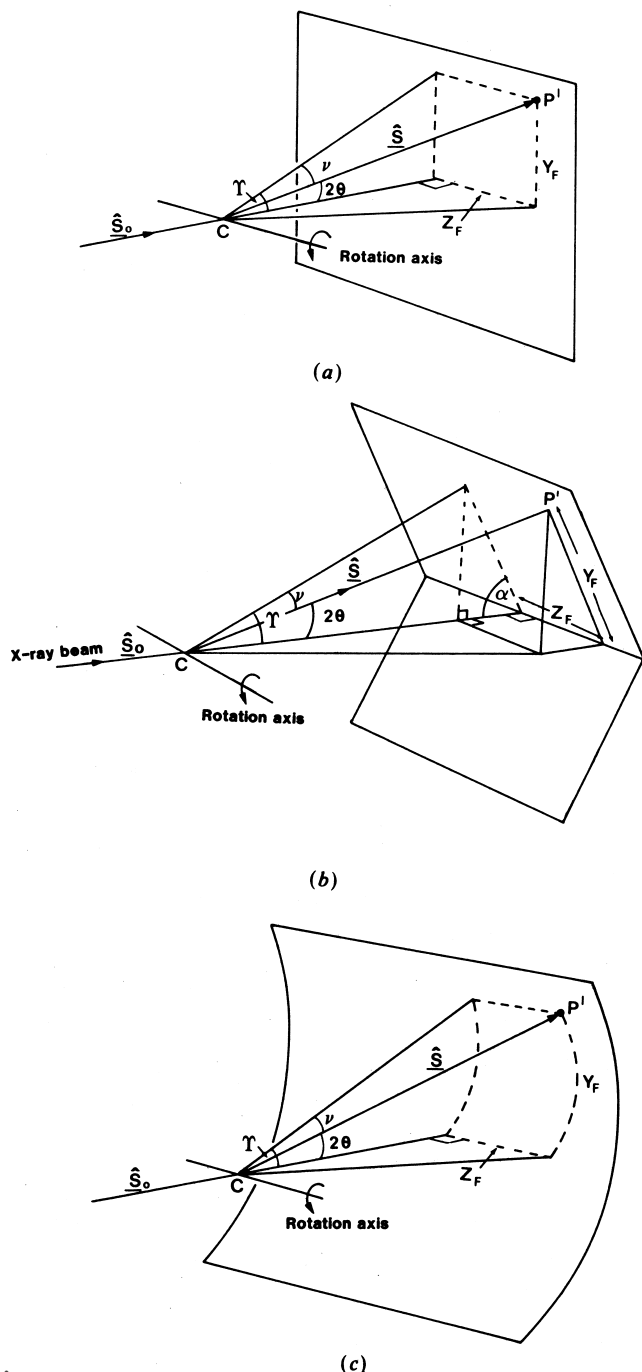


**Figure 7**  
Geometrical principles of recording the pattern on (a) a plane detector, (b) a V-shaped detector, (c) a cylindrical detector.

3.3. Relationship of reciprocal-lattice coordinates to crystal system parameters

The reciprocal-lattice coordinates  $\zeta, \xi, \Upsilon, \nu$  etc. used earlier, refer to an axial system fixed to the crystal,  $X_0Y_0Z_0$  of Fig. 8. Clearly, a given relp needs to be brought into the Ewald sphere by the rotation about the rotation axis. The treatment here follows Arndt & Wonacott (1977).

The rotation angle required,  $\varphi$ , is with respect to some reference 'zero-angle' direction and is determined by the particular crystal parameters. It is necessary to define a standard orientation of the crystal (*i.e.* datum) when  $\varphi = 0^\circ$ . If we define an axial system  $X_0Y_0Z_0$  fixed to the crystal and a laboratory axis system  $XYZ$  with  $X$  parallel to the beam and  $Z$  coincident with the rotation axis, then  $\varphi = 0^\circ$  corresponds to these axial systems being coincident (Fig. 8).

The angle of the crystal at which a given relp diffracts is

$$\tan(\varphi/2) = \frac{2y_0 \pm (4y_0^2 + 4x_0^2 - d^{*4})^{1/2}}{(d^{*2} - 2x_0)}. \quad (35)$$

The two solutions correspond to the two rotation angles at which the relp  $P$  cuts the sphere of reflection. Note that  $Y_F, Z_F$  (Section 3.2) are independent of  $\varphi$ .

The values of  $x_0$  and  $y_0$  are calculated from the particular crystal system parameters. The relationships between the coordinates  $x_0, y_0, z_0$  and  $\xi$  and  $\zeta$  are

$$\xi = (x_0^2 + y_0^2)^{1/2}, \quad (36)$$

$$\zeta = z_0. \quad (37)$$

$\mathbf{X}_0$  can be related to the crystal parameters by

$$\mathbf{X}_0 = \mathbf{A}\mathbf{h}. \quad (38)$$

$\mathbf{A}$  is a crystal-orientation matrix defining the standard datum orientation of the crystal.

For example, if, by convention,  $\mathbf{a}^*$  is chosen as parallel to the X-ray beam at  $\varphi = 0^\circ$  and  $\mathbf{c}$  is chosen as the rotation axis, then, for the general case,

$$\mathbf{A} = \begin{bmatrix} a^* & b^* \cos \gamma^* & c^* \cos \beta^* \\ 0 & b^* \sin \gamma^* & -c^* \sin \beta^* \cos \alpha \\ 0 & 0 & c^* \end{bmatrix}. \quad (39)$$

If the crystal is mounted on the goniometer head differently from this then  $\mathbf{A}$  can be modified by another matrix,  $\mathbf{M}$ , say, or the terms permuted. This exercise becomes clear if the reader takes an orthogonal case ( $\alpha = \beta = \gamma = 90^\circ$ ). For the general case, see Higashi (1989).

The crystal will most likely be misaligned (slightly or grossly) from the ideal orientation. To correct for this, the misorientation matrices  $\Phi_x, \Phi_y, \Phi_z$  are introduced, *i.e.*

$$\Phi_x = \begin{bmatrix} 1 & 0 & 0 \\ 0 & \cos \Delta\varphi_x & -\sin \Delta\varphi_x \\ 0 & \sin \Delta\varphi_x & \cos \Delta\varphi_x \end{bmatrix} \quad (40)$$

$$\Phi_y = \begin{bmatrix} \cos \Delta\varphi_y & 0 & \sin \Delta\varphi_y \\ 0 & 1 & 0 \\ -\sin \Delta\varphi_y & 0 & \cos \Delta\varphi_y \end{bmatrix} \quad (41)$$

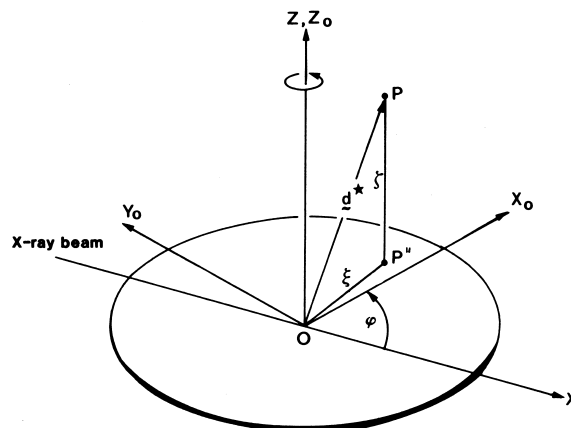


Figure 8 The rotation method. Definition of coordinate systems. [Cylindrical coordinates of a relp  $P$  ( $\xi, \zeta, \varphi$ ) are defined relative to the axial system  $X_0Y_0Z_0$  which rotates with the crystal.] The axial system  $XYZ$  is defined such that  $X$  is parallel to the incident beam and  $Z$  is coincident with the rotation axis. From Arndt & Wonacott (1977), reproduced with permission of Elsevier.

$$\Phi_z = \begin{bmatrix} \cos \Delta\varphi_z & -\sin \Delta\varphi_z & 0 \\ \sin \Delta\varphi_z & \cos \Delta\varphi_z & 0 \\ 0 & 0 & 1 \end{bmatrix}, \quad (42)$$

where  $\Delta\varphi_x, \Delta\varphi_y$  and  $\Delta\varphi_z$  are angles around the  $X_0, Y_0$  and  $Z_0$  axes, respectively.

Hence, the relationship between  $\mathbf{X}_0$  and  $\mathbf{h}$  is

$$\mathbf{X}_0 = \Phi_z \Phi_y \Phi_x \mathbf{M} \mathbf{A} \mathbf{h}. \quad (43)$$

An interesting method of auto-indexing, without and with knowledge of crystal unit-cell parameters, from a single, small rotation, monochromatic diffraction pattern is that of Higashi (1990). This method may have utility with the new X-ray lasers and a single still diffraction pattern measured from a nano-crystal.

3.4. Maximum oscillation angle without spot overlap

For a given oscillation photograph, there is a maximum value of the oscillation range,  $\Delta\varphi$ , that avoids overlapping of spots on a film. The overlap is most likely to occur in the region of the diffraction pattern perpendicular to the rotation axis and at the maximum Bragg angle. This is where relp's pass through the Ewald sphere with the greatest velocity. For such a separation between successive relp's of  $a^*$ , then the maximum allowable rotation angle to avoid spatial overlap is given by

$$\Delta\varphi_{\max} = \left[ \frac{a^*}{d_{\max}^*} - \Delta \right], \quad (44)$$

where  $\Delta$  is the sample reflecting range (see Section 7).  $\Delta\varphi_{\max}$  is a function of  $\varphi$ , even in the case of identical cell parameters. This is because it is necessary to consider, for a given orientation, the relevant reciprocal-lattice vector perpendicular to  $d_{\max}^*$ . In the case where the cell dimensions are quite different in magnitude (excluding the axis parallel to the rotation axis), then  $\Delta\varphi_{\max}$  is a marked function of the orientation.

In the rotation method several approaches are used. Firstly, as large an angle as possible is used up to  $\Delta\varphi_{\max}$ . This reduces the number of images that need to be processed and the number of partially stimulated reflections per image but at the expense of signal-to-noise ratio for individual spots, which accumulate more background since  $\Delta < \Delta\varphi_{\max}$ . Secondly,  $\Delta\varphi$  is chosen usually to be less than  $\Delta$  so as to optimize the signal-to-noise ratio of the measurement and to sample the rocking-width profile. A diffraction image is read after the crystal rotation has finished. As disk storage has become cheaper and detector device readout times shorter the use of ‘very fine phi slicing’ takes this approach of reflection profile measurement to the ideal limit. Thirdly, a continuous rotation scheme (‘shutterless data collection’) can be applied using pixel area detectors where each pixel can be read individually. Such schemes are also feasible with multiwire proportional chamber detectors (MWPCs).

The value of  $\Delta$ , the crystal rocking width for a given  $hkl$ , depends on the reciprocal-lattice coordinates of the  $hkl$  relp (see Section 7). In the region close to the rotation axis,  $\Delta$  is large.

In the introductory remarks to the monochromatic methods used, it has already been noted that originally the rotation method involved  $360^\circ$  rotations contributing to the diffraction image. Spot overlap led to loss of reflection data and encouraged Bernal and Weissenberg to devise improvements. With modern synchrotron techniques, the restriction on  $\Delta\varphi_{\max}$  [equation (44)] can be relaxed for special applications. For example, since the spot overlap that is to be avoided involves relp’s from adjacent reciprocal-lattice planes, the different Miller indices  $hkl$  and  $h + l, k, l$  do lead in fact to a small difference in Bragg angle. With good enough collimation, a small spot size exists at the detector plane so that the two spots can be resolved. For a standard-sized detector, this is practical for low-resolution data recording. Alternatively, a much larger detector can be contemplated and even medium-resolution data can be recorded without major overlap problems. These techniques could be useful in some time-resolved applications. For a discussion see Weisgerber & Helliwell (1993) and Helliwell (2005). For regular data collection, however, narrow angular ranges are preferred so as to reduce the background noise in the diffraction images and also to avoid loss of any data because of spot overlap.

### 3.5. Blind region

In normal-beam geometry, any relp lying close to the rotation axis will not be stimulated at all. This situation is shown in Fig. 9. The blind region has a radius of

$$\xi_{\min} = d_{\max}^* \sin \theta_{\max} = \frac{\lambda^2}{2d_{\min}^2}, \quad (45)$$

and is therefore strongly dependent on  $d_{\min}$  but can be ameliorated by use of a short  $\lambda$ . Shorter  $\lambda$  makes the Ewald sphere have a larger radius, *i.e.* its surface moves closer to the rotation axis. At Cu  $K\alpha$  for 2 Å resolution, approximately 5% of the data lie in the blind region according to this simple

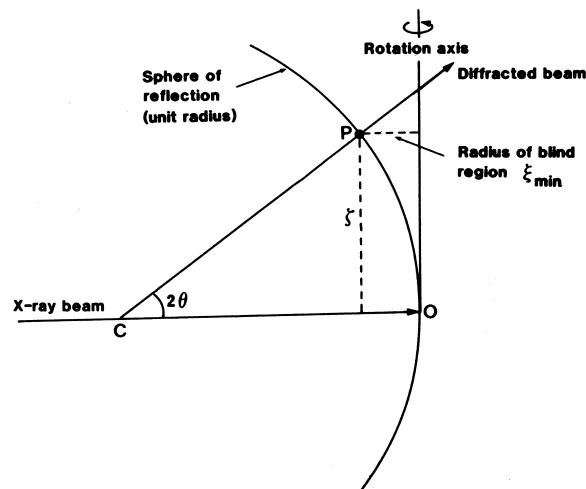


Figure 9

The rotation method. The blind region associated with a single rotation axis. From Arndt & Wonacott (1977), reproduced with permission of Elsevier.

geometrical model. However, taking account of the rocking width  $\Delta$ , a slightly greater percentage of the data than this is not fully sampled except over very large angular ranges. The actual increase in the blind-region volume due to this effect is minimized by use of a collimated beam and a narrow spectral spread (*i.e.* finely monochromated, synchrotron radiation) if the crystal is not too mosaic.

These effects are directly related to the Lorentz factor,

$$L = 1/(\sin^2 2\theta - \zeta^2)^{1/2}. \quad (46)$$

It is inadvisable to measure a reflection intensity when  $L$  is large because different parts of a spot would need a different Lorentz factor, which is unrealistic.

The blind region can be filled in by a rotation about another axis. The total angular range that is needed to sample the blind region is  $2\theta_{\max}$  in the absence of any symmetry or  $\theta_{\max}$  in the case of  $mm$  symmetry (for example). With crystals of high enough symmetry, *i.e.* not triclinic, and use of a random orientation, complete sampling of the unique region of reciprocal space can be obtained from a single rotation axis setting. However, for precise anomalous scattering measurements careful setting of the crystal orientation is often preferred (see *e.g.* Einspahr *et al.*, 1985; Nieh & Helliwell, 1995) and thus rotation about another axis to capture the blind-region missing data will be required. A reciprocal-lattice viewer of a processed diffraction data set, so as to scrutinize gaps in the measurements, is available at <https://stارانiso.globalphasing.org/cgi-bin/PDBpeep.cgi> (Tickle *et al.*, 2021).

## 4. Weissenberg geometry

Weissenberg geometry (Weissenberg, 1924) is dealt with in the books by Buerger (1942) and Woolfson (1970, 1997), for example.

## 4.1. General

The conventional Weissenberg method uses a moving film in conjunction with the rotation of the crystal and a layer-line screen. This allows:

(a) A larger rotation range of the crystal to be used (say  $200^\circ$ ), avoiding the problem of overlap of reflections (referred to in Section 3.4 on oscillation photography).

(b) Indexing of reflections on the photograph to be made by inspection.

The Weissenberg method is not widely used now. In small-molecule crystallography, quantitative data collection is usually performed by means of a CCD area-detector diffractometer.

Weissenberg geometry has been revived as a method for macromolecular data collection at the Photon Factory (Sakabe, 1983, 1991), exploiting monochromated synchrotron radiation and the image plate as detector. Here the method is used without a layer-line screen where the total rotation angle is limited to  $\sim 15^\circ$ ; this is a significant increase over the rotation method with a stationary film. The use of this effectively avoids the presence of partial reflections and reduces the total number of exposures required. Provided the Weissenberg camera has a large radius, the X-ray background accumulated over a single spot is actually not as serious as one might fear. This is because the X-ray background decreases approximately according to the inverse square of the distance from the crystal to the detector. For very weakly scattering crystals owing to very small sample size or large unit cell *etc.* this will of course become a real limitation. However, the use of such a camera has not been widely adopted at other synchrotron facilities.

The following Sections 4.2 and 4.3 describe the standard situation where a layer-line screen is used.

## 4.2. Recording of zero layer

Normal-beam geometry (*i.e.* the X-ray beam perpendicular to the rotation axis) is used to record zero-layer photographs. The film is held in a cylindrical cassette coaxial with the rotation axis. The centre of the gap in a screen is set to coincide with the zero-layer plane. The coordinate of a spot on the film measured parallel ( $Z_F$ ) and perpendicular ( $Y_F$ ) to the rotation axis is given by

$$Y_F = \frac{2\pi}{360} D\Upsilon \quad (47)$$

$$Z_F = \varphi/f, \quad (48)$$

where  $\varphi$  is the rotation angle of the crystal from its initial setting,  $f$  is the coupling constant, which is the ratio of the crystal rotation angle divided by the film cassette translation distance, in  $^\circ \text{ min}^{-1}$ , and  $D$  is the camera radius. Generally, the values of  $f$  and  $D$  are  $2^\circ \text{ min}^{-1}$  and 28.65 mm, respectively.

## 4.3. Recording of upper layers

Upper-layer photographs are usually recorded in equi-inclination geometry [*i.e.*  $\mu = -\nu$  in equations (21) and (22)].

The X-ray-beam direction is made coincident with the generator of the cone of the diffracted beam for the layer concerned, so that the incident and diffracted beams make equal angles ( $\mu$ ) with the equatorial plane, where

$$\mu = \sin^{-1} \zeta_n/2. \quad (49)$$

The screen has to be moved by an amount

$$s \tan \mu, \quad (50)$$

where  $s$  is the screen radius. If the cassette is held in the same position as the zero-layer photograph, then reflections produced by the same orientation of the crystal will be displaced

$$D \tan \mu \quad (51)$$

relative to the zero-layer photograph. This effect can be eliminated by initial translation of the cassette by  $D \tan \mu$ .

## 5. Precession geometry

The main book dealing with the precession method is that of Buerger (1964) and is now of largely historical interest. The advantage of the precession method was that it gave an undistorted view of the reciprocal lattice because it used a flat film cassette geometry, but it did not show as many reflections as the Weissenberg method. Today a 'virtual precession photo' of a zero layer is harnessed in validation checks of the diffraction data. These checks can be readily calculated and the results readily displayed; such checks show up missing regions of the measured diffraction data. The mtz processed diffraction file viewer in the CCP4 program suite (<https://www.ccp4.ac.uk/>) has a utility that provides this graphic visualization functionality.

### 5.1. General

The precession method with a layer-line screen is used to record an undistorted representation of a single plane of relp's and their associated intensities. In order to achieve this, the crystal is carefully set so that the plane of relp's is perpendicular to the X-ray beam. The normal to this plane, the zone axis, is then precessed about the X-ray-beam axis. A layer-line screen allows only relp's of the plane of interest to pass through to the film. The motion of the crystal, screen and film are coupled together to maintain the coplanarity of the film, screen and zone. For X-rays this is now of mainly historical interest in that the precession camera is rarely used. However an undistorted view of a single plane of relp's and their associated intensities is still valuable and can be readily created from intensity measurements made with the rotation method and a diffractometer, as described above. With electrons there has been a renewed interest in the precession method (without a layer-line screen) since it improves the measured values of the electron intensity, which are basically free from dynamical effects (Vincent & Midgley, 1994). This is being applied to nano- and microcrystals of small molecules (see *e.g.* Nicolopoulos *et al.*, 2007) and proteins (see *e.g.* Georgieva *et al.*, 2008). This is complemented with rotation

**Table 2**

The distance displacement (in mm) measured on the film versus angular setting error of the crystal for a screenless precession ( $\bar{\mu} = 5^\circ$ ) setting photograph.

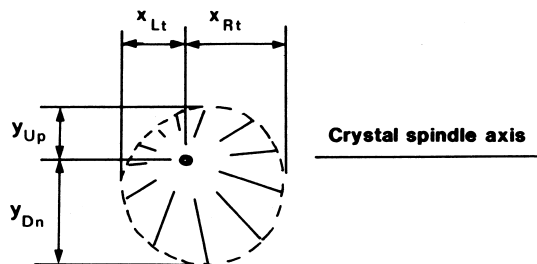
Alternatively,  $\Delta = \delta/D \simeq \sin 4\varepsilon$  can be used if  $\varepsilon$  is small [from equation (52)]. *Notes:* (1) A value of  $\bar{\mu}$  of  $5^\circ$  is assumed, although there is a negligible variation in  $\varepsilon$  with  $\bar{\mu}$  between  $3^\circ$  (typical for proteins) and  $7^\circ$  (typical for small molecules). (2) Crystal-to-film distances on a precession camera are usually settable at the fixed distance  $D = 60, 75$  and  $100$  mm. (3) This table should be used in conjunction with Fig. 10. (4) Values of  $\varepsilon$  are given in intervals of  $5'$  as this is convenient for various goniometer heads which usually have verniers in  $5', 6'$  or  $10'$  units. The vernier on the spindle of the precession camera is often in  $2'$  units.

Angular correction, $\varepsilon$ , in degrees and minutes	$\Delta$ r.l.u.	Distance displacement (mm) for three crystal-to-film distances		
		60 mm	75 mm	100 mm
0	0	0	0	0
15'	0.0175	1.1	1.3	1.8
30'	0.035	2.1	2.6	3.5
45'	0.0526	3.2	4.0	5.3
60'	0.070	4.2	5.3	7.0
1° 15'	0.087	5.2	6.5	8.7
1° 30'	0.105	6.3	7.9	10.5
1° 45'	0.123	7.4	9.2	12.3
2°	0.140	8.4	10.5	14.0

electron crystallography geometry (see Fig. 2 of Gemmi *et al.*, 2019). Gemmi *et al.* (2019) also provide an up-to-date exposition and review of electron crystallography methods, analyses and results.

## 5.2. Crystal setting

Setting of the crystal for one zone is carried out in two stages. First, a monochromatic still identifies the required zone axis, which is placed parallel to the X-ray beam. This is done by adjustment to the camera-spindle angle and the goniometer-head arc in the horizontal plane. This procedure is usually accurate to a degree or so. Note that the vertical arc will only rotate the pattern around the X-ray beam. Second, a screenless precession photograph is taken using an angle of  $\sim 7$ – $10^\circ$  for small molecules or  $2$ – $3^\circ$  for macromolecules. It is better to use unfiltered radiation, as then the edge of the zero-layer circle is easily visible. Let the difference of the distances from the centre of the pattern to the opposite edges of the trace in the direction of displacement be called  $\delta = D\Delta$  so that

**Figure 10**

The screenless precession setting photograph (schematic) and associated mis-setting angles for a typical orientation error when the crystal has been set previously by a monochromatic still.

for the horizontal goniometer-head arc and the dial:  $\delta_{\text{arc}} = x_{\text{Rt}} - x_{\text{Lt}}$  and  $\delta_{\text{dial}} = y_{\text{Up}} - y_{\text{Dn}}$  (Fig. 10). The corrections  $\varepsilon$  to the arc and camera spindle are given by

$$\Delta = \frac{\delta}{D} = \frac{\sin 4\varepsilon \cos \bar{\mu}}{\cos^2 2\varepsilon - \sin^2 \bar{\mu}} \text{ in r.l.u.}, \quad (52)$$

where  $D$  is the crystal-to-film distance and  $\bar{\mu}$  is the precession angle.

It is possible to measure  $\delta$  to about  $0.3$  mm ( $\delta = 1$  mm corresponds to  $14'$  error for  $D = 60$  mm and  $\bar{\mu} \simeq 7^\circ$  [Table 2, based on *International Tables for X-ray Crystallography* Vol. II (1959, p. 200)]).

## 5.3. Recording of zero-layer photograph

Before the zero-layer photograph is taken, an Nb filter (for Mo  $K\alpha$ ) or an Ni filter (for Cu  $K\alpha$ ) is introduced into the X-ray beam path and a screen is placed between the crystal and the film at a distance from the crystal of

$$s = r_s \cot \bar{\mu}, \quad (53)$$

where  $r_s$  is the screen radius. Typical values of  $\bar{\mu}$  would be  $20^\circ$  for a small molecule with Mo  $K\alpha$  and  $12$ – $15^\circ$  for a protein with Cu  $K\alpha$ . The annulus width in the screen is chosen usually as  $2$ – $3$  mm for a small molecule and  $1$ – $2$  mm for a macromolecule. A clutch slip allows the camera motor to be disengaged and the precession motion can be executed under hand control to check for fouling of the goniometer head, crystal, screen or film cassette;  $s$  and  $r_s$  need to be selected so as to avoid this happening. The zero-layer precession photograph produced has a radius of  $2D \sin \bar{\mu}$  corresponding to a resolution limit  $d_{\text{min}} = \lambda/2 \sin \bar{\mu}$ . The distance between spots  $A$  is related to the reciprocal-cell parameter  $a^*$  by the formula

$$a^* = \frac{A}{D}. \quad (54)$$

## 5.4. Recording of upper-layer photographs

The recording of upper-layer photographs involves isolating the net of relp's at a distance from the zero layer of  $\zeta_n = n\lambda/b$ , where  $b$  is the case of the  $b$  axis antiparallel to the X-ray beam. In order to determine  $\zeta_n$ , it is generally necessary to record a cone-axis photograph. If the cell parameters are known, then the camera settings for the upper-level photograph can be calculated directly without the need for a cone-axis photograph.

In the upper-layer precession photograph, the film is advanced towards the crystal by a distance

$$D\zeta_n \quad (55)$$

and the screen is placed at a distance

$$s_n = r_s \cot \bar{\nu}_n = r_s \cot \cos^{-1}(\cos \bar{\mu} - \zeta_n). \quad (56)$$

The resulting upper-layer photograph has outer radius

$$D(\sin \bar{\nu}_n + \sin \bar{\mu}) \quad (57)$$

and an inner blind region of radius

$$D(\sin \bar{\nu}_n - \sin \bar{\mu}). \tag{58}$$

5.5. Recording of cone-axis photograph

A cone-axis photograph (or screenless precession diffraction image) is recorded by using a small precession angle, *e.g.* 5° for a small molecule or 1° for a protein. The diffraction image has the appearance of concentric circles centred on the origin of reciprocal space, provided the crystal is perfectly aligned. The radius of each circle is

$$r_n = s \tan \bar{\nu}_n, \tag{59}$$

where

$$\cos \bar{\nu}_n = \cos \bar{\mu} - \zeta_n. \tag{60}$$

Hence,  $\zeta_n = \cos \bar{\mu} - \cos \tan^{-1}(r_n/s)$ .

6. Diffractometry

The main book devoted to single-crystal diffractometry is that of Arndt & Willis (1966). An extensive description is also given in Aslanov *et al.* (1998). Hamilton (1974) gives a detailed treatment of angle settings for four-circle diffractometers. For details of area-detector diffractometry, see Howard *et al.* (1985), Hamlin (1985) and Dauter & Wilson (2001).

6.1. General

In this section, we describe the following related diffractometer configurations:

- (a) multiple axes [ $\omega$ ,  $\chi$ ,  $\varphi$  option or  $\omega$ ,  $\kappa$ ,  $\varphi$  (kappa) option];
- (b) fixed  $\chi = 45^\circ$  geometry with area detector.

Configuration (a) is used with single-counter and area detectors. Configuration (b) is used with area detectors.

The purpose of the diffractometer goniostat is to bring a selected reflected beam into the detector aperture or a number of reflected beams onto an area detector of limited

aperture (*i.e.* an aperture that does not intercept all the available diffraction spots at one setting of the area detector) [see Hamlin (1985), p. 431, for example] or for crystal alignment for the most precise anomalous scattering measurements. The use of electronic area detectors is now the most widespread.

The single-counter diffractometer used to be the primary device for small-molecule crystallography. In macromolecular crystallography, many relp's are almost simultaneously in the diffraction condition. The single-counter diffractometer was extended to five separate counters [for a review, see Artymiuk & Phillips (1985)], then subsequently to a multi-element linear detector [for a review, see Wlodawer (1985)]. Area detectors offered an even larger aperture for simultaneous acquisition of reflections [Hamlin *et al.* (1981), and references therein]. The CCDs or image plates have to a great extent been succeeded by the pixel area detectors (for an early reference see Broennimann *et al.*, 2006).

6.2. Multiple axes geometry

With a multiple axes geometry (Fig. 11), a crystal can be oriented specifically so as to bring the incident and reflected beams, for a given relp, into the equatorial plane. In this way, the detector is moved to intercept the reflected beam by a single rotation movement about a vertical axis (the  $2\theta$  axis). The value of  $\theta$  is given by Bragg's law. In order to bring  $\mathbf{d}^*$  into the equatorial plane (*i.e.* the Bragg plane into the meridional plane), suitable angular settings of a three-axis goniostat are necessary. The convention for the sign of the angles given in Fig. 11 is that of Hamilton (1974); his choice of sign of  $2\theta$  is adhered to despite the fact that it is left-handed, but in any case the signs of  $\omega$ ,  $\chi$ ,  $\varphi$  are standard right-handed. The specific reciprocal-lattice point can be rotated from point *P* to point *Q* by the  $\varphi$  rotation, from *Q* to *R* via  $\chi$ , and *R* to *S* via  $\omega$  (see Fig. 12).

In the most commonly used setting, the  $\chi$  plane bisects the incident and diffracted beams at the measuring position.

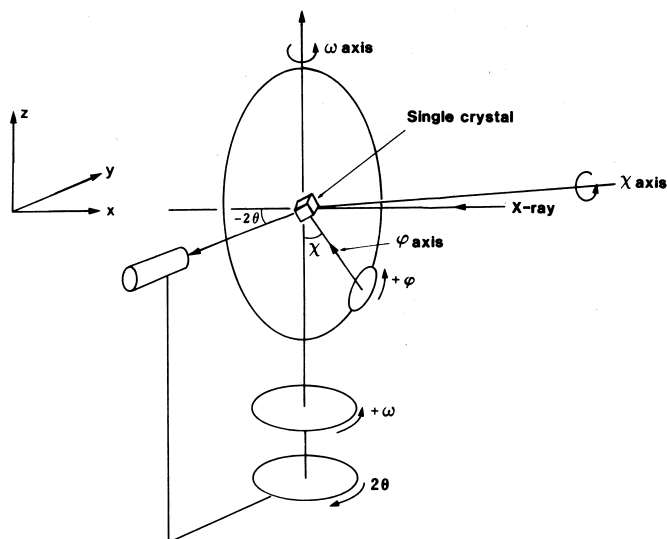


Figure 11 Normal-beam equatorial geometry: the angles  $\omega$ ,  $\chi$ ,  $\varphi$ ,  $2\theta$  are drawn in the convention of Hamilton (1974).

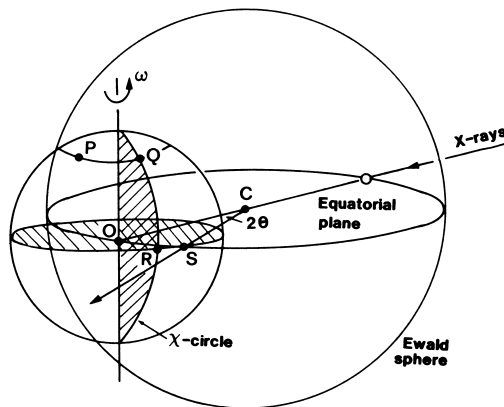


Figure 12 Diffractometry with normal-beam equatorial geometry and angular motions  $\omega$ ,  $\chi$  and  $\varphi$ . The relp at *P* is moved to *Q* via  $\varphi$ , from *Q* to *R* via  $\chi$ , and *R* to *S* via  $\omega$ . From Arndt & Willis (1966). Reproduced with permission of Cambridge University Press through PLSclear. In this specific example, the  $\varphi$  axis is parallel to the  $\omega$  axis (*i.e.*  $\chi = 0^\circ$ ).

Hence, the vector  $\mathbf{d}^*$  lies in the  $\chi$  plane at the measuring position. However, since it is possible for reflection to take place for any orientation of the reflecting plane rotated about  $\mathbf{d}^*$ , it is feasible therefore that  $\mathbf{d}^*$  can make any arbitrary angle  $\varepsilon$  with the  $\chi$  plane. It is conventional to refer to the azimuthal angle  $\psi$  of the reflecting plane as the angle of rotation about  $\mathbf{d}^*$ . It is possible with a  $\psi$  scan to keep the  $hkl$  reflection in the diffraction condition and so to measure the sample absorption surface by monitoring the variation in intensity of this reflection. This  $\psi$  scan is achieved by adjustment of the  $\omega$ ,  $\chi$ ,  $\varphi$  angles. When  $\chi = \pm 90^\circ$ , the  $\psi$  scan is simply a  $\varphi$  scan and  $\varepsilon$  is  $0^\circ$ .

The  $\chi$  circle is a relatively bulky object whose thickness can inhibit the measurement of diffracted beams at high  $\theta$ . Also, collision of the  $\chi$  circle with the collimator or X-ray-tube housing has to be avoided. An alternative is the kappa goniostat geometry. In the kappa diffractometer [for a schematic picture, see Wyckoff (1985, p. 334)], the  $\kappa$  axis is inclined at  $50^\circ$  to the  $\omega$  axis and can be rotated about the  $\omega$  axis; the  $\kappa$  axis is an alternative to  $\chi$  therefore. The  $\varphi$  axis is mounted on the  $\kappa$  axis. In this way, an unobstructed view of the sample is achieved.

### 6.3. Fixed- $\chi$ geometry with area detector

The geometry with fixed  $\chi$  consists of an  $\omega$  axis, a  $\varphi$  axis and  $\chi$  fixed. The rotation axis is the  $\omega$  axis. In this configuration, it is possible to sample a greater number of independent reflections per degree of rotation (*e.g.* see Xuong *et al.*, 1985) because of the generally random nature of any symmetry axis. For small-molecule crystallography fixed- $\chi$  instruments have  $\chi = 54.74^\circ$ , known as the ‘magic angle’, as it provides a complete sphere of reciprocal space which can be collected by a set of three  $180^\circ$   $\omega$  scans at three different settings; the Bruker ‘SC-XRD’ fixed- $\chi$  goniometer has this geometry. The angle of  $54.74^\circ$  chosen in such an apparatus is the angle between the body diagonal of a cube and the edges of the cube.

## 7. Practical realization of diffraction geometry: sources, optics and detectors

### 7.1. General

The tools required for making the necessary measurement of reflection intensities include beam-conditioning items, crystal goniostat and detectors.

In this section, we describe the common configurations for defining precise states of the X-ray beam. The topic of detectors is dealt with in Part 7 of the previous edition of *International Tables for Crystallography*, Vol. C (2006) (see especially Section 7.1.6). The impact of detector distortions on diffraction geometry is dealt with below in Section 7.4 of this present chapter.

Within the topic of beam conditioning the following subtopics are dealt with: (a) collimation, (b) monochromators and (c) mirrors.

An exhaustive survey is not given, since a wide range of configurations are feasible. Instead, the commonest arrange-

ments are covered. In addition, conventional X-ray sources are separated from synchrotron X-ray sources. The important difference in the treatment of the two types of source is that on the synchrotron the position and angle of the photon emission from the relativistic charged particles are correlated. One result of this, for example, is that after monochromatization of the synchrotron radiation (SR) the wavelength and angular direction of a photon are correlated. With X-ray undulators the divergence angles, in both the horizontal and vertical directions, are very small *e.g.*  $\sim 20 \mu\text{rad}$ .

The angular reflecting range and diffraction-spot size are determined by the physical state of the beam and the sample. *Hence, the idealized situation considered earlier of a point sample and zero-divergence beam will be relaxed.* Moreover, the effects of the detector-imaging characteristics are considered, *i.e.* obliquity, parallax, point-spread factor and spatial distortions.

### 7.2. Conventional X-ray sources: spectral character, crystal rocking curve and spot size

An extended discussion of instrumentation relating to conventional X-ray sources is given in Arndt & Willis (1966) and Arndt & Wonacott (1977). Witz (1969) has reviewed the use of monochromators for conventional X-ray sources. See also Aslanov *et al.* (1998).

It is generally the case that the  $K\alpha$  line has been used for single-crystal data collection *via* monochromatic methods. The continuum *Bremsstrahlung* radiation has been used for Laue photography usually at the stage of setting crystals but also used extensively for structure analysis from 1913 through to the 1920s and 1930s very notably by W. L. Bragg, R. G. Dickinson, S. Nishikawa, L. Pauling and R. W. G. Wyckoff (for a history of this period see Cruickshank, 1992).

The emission lines of interest consist of the  $K\alpha_1$ ,  $K\alpha_2$  doublet and the  $K\beta$  line. The intrinsic spectral width of the  $K\alpha_1$  or  $K\alpha_2$  line is  $\sim 10^{-4}$ , their separation ( $\delta\lambda/\lambda$ ) is  $2.5 \times 10^{-3}$ , and they are of different relative intensity. The  $K\beta$  line is eliminated either by use of a suitable metal filter or by a monochromator. A mosaic monochromator such as graphite passes the  $K\alpha_1$ ,  $K\alpha_2$  doublet in its entirety. The monochromator passes a certain, if small, component of a harmonic of the  $K\alpha_1$ ,  $K\alpha_2$  line extracted from the *Bremsstrahlung*. This latter effect only becomes important in circumstances where the *attenuated* main beam is used for calibration; the process of attenuation enhances the short-wavelength harmonic component to a significant degree. In diffraction experiments, this component is of negligible intensity. The polarization correction is different with and without a monochromator [see the previous edition of *International Tables for Crystallography*, Vol. C (2006), Chapter 6.2].

The effect of the doublet components of the  $K\alpha$  emission is to cause a peak broadening at high angles. From Bragg’s law, the following relationship holds for a given reflection:

$$\delta\theta = \frac{\delta\lambda}{\lambda} \tan \theta. \quad (61)$$

For proteins where  $\theta$  is relatively small, the effect of the  $K\alpha_1$ ,  $K\alpha_2$  separation is generally not significant. For small molecules, which diffract to higher resolution, this is a significant effect and has to be accounted for at high angles.

The width of the rocking curve of a crystal reflection is given by (Arndt & Willis, 1966)

$$\Delta = \left\{ \left[ \frac{a+f}{s} \right] + \eta + \frac{\delta\lambda}{\lambda} \tan \theta \right\} \quad (62)$$

when the crystal is fully bathed by the X-ray beam, where  $a$  is the crystal size,  $f$  the X-ray tube focus size (foreshortened),  $s$  the distance between the X-ray tube focus and the crystal, and  $\eta$  the crystal mosaic spread (Fig. 13).

In the moving-crystal method,  $\Delta$  is the minimum angle through which the crystal must be rotated, for a given reflection,

so that every mosaic block can diffract radiation covering a fixed wavelength band  $\delta\lambda$  from every point on the focal spot.

This angle  $\Delta$  can be controlled to some extent, for the protein case, by collimation. For example, with a collimator entrance slit placed as close to the X-ray tube as possible and a collimator exit slit placed as close to the sample as possible, the value of  $(a+f)/s$  can approximately be replaced by  $(a'+f')/s'$ , where  $f'$  is the entrance-slit size,  $a'$  is the exit-slit size, and  $s'$  the distance between them. Clearly, for  $a' < a$ , the whole crystal is no longer bathed by the X-ray beam. In fact, by simply inserting horizontal and vertical adjustable screws at the front and back of the collimator, adjustment to the horizontal and vertical divergence angles can be made. The spot size at the detector can be calculated approximately by multiplying the particular reflection rocking angle  $\Delta$  by the distance from the sample to the spot on the detector. In the case of a single-counter diffractometer, tails on a diffraction spot can be eliminated by use of a detector collimator.

Spot-to-spot spatial resolution can be enhanced by use of focusing mirrors, which is especially important for large-protein and virus crystallography, where long cell axes occur. The effect is achieved by focusing the beam on the detector, thereby changing a divergence from the source into a convergence to the detector.

In the absence of absorption, at grazing angles, X-rays up to a certain critical energy are reflected. The critical angle  $\theta_c$  is given by

$$\theta_c = \left[ \frac{e^2 N}{mc^2 \pi} \right]^{1/2} \lambda, \quad (63)$$

where  $N$  is the number of free electrons per unit volume of the reflecting material. The higher the atomic number of a given material then the larger is  $\theta_c$  for a given critical wavelength. The product of mirror aperture with reflectivity gives a figure of merit for the mirror as an efficient optical element.

The use of a pair of perpendicular curved mirrors set in the horizontal and vertical planes can focus the X-ray tube source to a small spot at the detector. The angle of the mirror to the incident beam is set to reject the  $K\beta$  line (and shorter-wavelength *Bremsstrahlung*). Hence, spectral purity at the sample and diffraction spot size at the detector are improved simultaneously. There is some loss of intensity (and lengthening of exposure time) but the overall signal-to-noise ratio is improved. Another reason for doing this, however, is to enhance spot-to-spot spatial resolution. The rocking width of the sample is not affected in the case of 1:1 focusing (object distance = image distance).

- To summarize, the configurations are
- (a) beam collimator only;
  - (b) filter + beam collimator;
  - (c) filter + beam collimator + detector collimator (single-counter case);
  - (d) graphite monochromator + beam collimator;
  - (e) pair of focusing mirrors + exit-slit assembly;
  - (f) focusing germanium monochromator + perpendicular focusing mirror + exit-slit assembly.

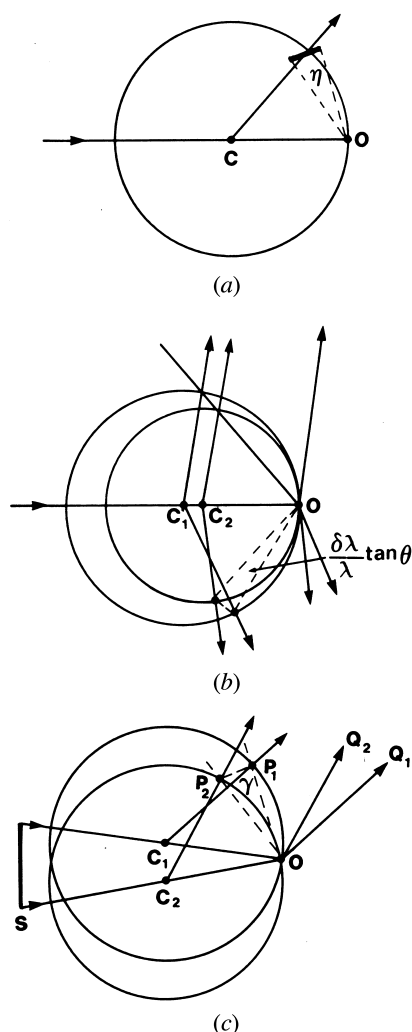


**Figure 13** Reflection rocking width for a conventional X-ray source. From Arndt & Wonacott (1977, p. 7), reproduced with permission of Elsevier. (a) Effect of sample mosaic spread. The relp is replaced by a spherical cap with a centre at the origin of reciprocal space where it subtends an angle  $\eta$ . (b) Effect of  $(\delta\lambda/\lambda)_{conv}$ , the conventional source type spectral spread. (c) Effect of a beam divergence angle,  $\gamma$ . The overall reflection rocking width is a combination of these effects.

Configuration (a) is for Laue mode; (b)–(f) are for monochromatic mode; (f) can also be applied to conventional-source work.

### 7.3. Synchrotron X-ray sources

In the utilization of synchrotron X-radiation (SR), both Laue and monochromatic modes are important for data collection. The unique geometric and spectral properties of SR renders the treatment of diffraction geometry different from that for a conventional X-ray source. The properties of SR are dealt with in the previous edition of *International Tables for Crystallography*, Vol. C (2006), Section 4.2.1.5 and elsewhere; see also the Subject Index of that edition. Reviews of instrumentation, methods and applications of synchrotron radiation in protein crystallography are given by Helliwell (1984, 1992).

(a) *Laue geometry: sources, optics, sample reflection bandwidth and spot size.* Laue geometry involves the use of the polychromatic SR spectrum as transmitted through the beryllium window that is often used to separate the apparatus from the machine vacuum. There is useful intensity down to a wavelength minimum of  $\sim\lambda_c/5$ , where  $\lambda_c$  is the critical wavelength of the magnet source. The maximum wavelength is typically  $\geq 3 \text{ \AA}$ ; however, if the crystal is mounted in a capillary then the glass absorbs the wavelengths beyond  $\sim 2.6 \text{ \AA}$ .

The bandwidth can be limited by optical elements. A reflecting mirror at grazing incidence can be used for two reasons. First, the minimum wavelength in the beam can be sharply defined to aid the accurate definition of the Laue-spot multiplicity. Second, the mirror can be used to focus the beam at the sample. The maximum-wavelength limit can be truncated by use of aluminium absorbers of varying thickness or by use of a transmission mirror (Lairson & Bilderback, 1982; Cassetta *et al.*, 1993). The case of undulator or wiggler-undulator ('wundulator') Laue is described below.

The measured intensity of individual Laue diffraction spots depends on the wavelength at which they are stimulated. The problem of wavelength normalization is treated by a variety of methods. These include:

- (a) use of a monochromatic reference data set;
- (b) use of symmetry equivalents and/or reflections recorded more than once in the Laue data set and measured at different wavelengths;
- (c) calibration with a standard sample such as a silicon crystal.

Each of these methods produces a ' $\lambda$ -curve' describing the relative strength of spots measured at various wavelengths. The methods rely on the incident spectrum being smooth and stable with time. There are discontinuities in the ' $\lambda$ -curve' at the bromine and silver *K*-absorption edges owing to the silver bromide in the photographic emulsion case. The  $\lambda$ -curve is then split up into wavelength regions, *i.e.*  $\lambda_{\min}$  to  $0.49 \text{ \AA}$ ,  $0.49$  to  $0.92 \text{ \AA}$ , and  $0.92 \text{ \AA}$  to  $\lambda_{\max}$ . Other detector types have different discontinuities, depending on the material making up the X-ray absorbing medium. [The quantification

of conventional-source Laue-diffraction data (Rabinovich & Lourie, 1987; Brooks & Moffat, 1991) requires the elimination of spots recorded near the emission-line wavelengths.]

The production and use of narrow-bandpass beams has increased in interest, *e.g.*  $\delta\lambda/\lambda \leq 0.2$  so as to maximize intensity signal to noise. An X-ray undulator of 10–100 periods ideally should yield a bandwidth behind a pinhole of  $\delta\lambda/\lambda \simeq 0.1$ – $0.01$ . By using a slightly stronger magnetic field a hybrid device wiggler-undulator ('wundulator') can be used to produce broader 'narrow-bandpass'. In these cases, wavelength normalization is more difficult because the actual spectrum over which a reflection is integrated is more rapidly varying in intensity, but modern Laue software caters for that (see Ren *et al.*, 1999; Arzt *et al.*, 1999; and Šrajcar *et al.*, 2000). The spot bandwidth is determined by the mosaic spread and horizontal beam divergence (since  $\gamma_H > \gamma_V$ ) as

$$\left[ \frac{\delta\lambda}{\lambda} \right] = (\eta + \gamma_H) \cot \theta, \quad (64)$$

where  $\eta$  = sample mosaic spread, assumed to be isotropic,  $\gamma_H$  = horizontal cross-fire angle, which in the absence of focusing is  $(x_H + \sigma_H)/P$ , where  $x_H$  is the horizontal sample size and  $\sigma_H$  the horizontal source size, and  $P$  is the sample to the tangent-point distance; and similarly for  $\gamma_V$  in the vertical direction. Generally, at SR sources,  $\sigma_H$  is greater than  $\sigma_V$ . When a focusing-mirror element is used,  $\gamma_H$  and/or  $\gamma_V$  are convergence angles determined by the focusing distances and the mirror aperture.

The size and shape of the diffraction spots vary across the detector plane. The radial spot length is given by convolution of Gaussians as

$$(L_R^2 + L_c^2 \sec^2 2\theta)^{1/2} \quad (65)$$

and tangentially by

$$(L_T^2 + L_c^2)^{1/2}, \quad (66)$$

where  $L_c$  is the size of the X-ray beam (assumed circular for simplicity) at the sample, and

$$L_R = D \sin(2\eta + \gamma_R) \sec^2 2\theta \quad (67)$$

$$L_T = D(2\eta + \gamma_T) \sin \theta \sec 2\theta, \quad (68)$$

and

$$\gamma_R = \gamma_V \cos \psi + \gamma_H \sin \psi \quad (69)$$

$$\gamma_T = \gamma_V \sin \psi + \gamma_H \cos \psi, \quad (70)$$

where  $\psi$  is the angle between the vertical direction and the radius vector to the spot (see Andrews *et al.*, 1987). For a crystal that is not too mosaic, the spot size is dominated by  $L_c$ . For a mosaic or radiation-damaged crystal, the main effect is a radial streaking arising from  $\eta$ , the sample mosaic spread.

(b) *Monochromatic SR beams: optical configurations and sample rocking width.* A wide variety of perfect-crystal monochromator configurations are possible and have been reviewed by various authors (Hart, 1971; Bonse *et al.*, 1976; Hastings, 1977; Kohra *et al.*, 1978). Since the reflectivity of

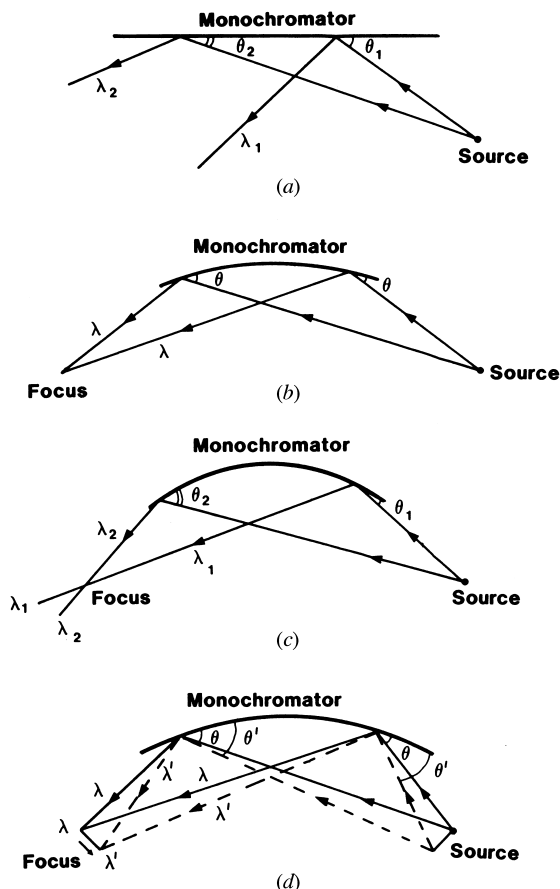


**Figure 14** Single-crystal monochromator illuminated by synchrotron radiation: (a) flat crystal, (b) Guinier setting, (c) overbent crystal, (d) effect of source size (shown at the Guinier setting for clarity). From Helliwell (1984). Copyright IOP Publishing. Reproduced with permission. All rights reserved.

perfect silicon and germanium is effectively 100%, multiple-reflection monochromators are feasible and permit the tailoring of the shape of the monochromator resolution function, harmonic rejection, and manipulation of the polarization state of the beam. Two basic designs are in common use. These are (a) the bent single-crystal monochromator of triangular shape (Lemonnier *et al.*, 1978) and (b) the double-crystal monochromator, either linked in a ‘channel cut’ device or as separate crystals.

In the case of the single-crystal monochromator, the actual curvature employed is very important in the diffraction geometry. For a point source and a flat monochromator crystal, there is a gradual change in the photon wavelength selected from the white beam as the length of the monochromator is traversed [Fig. 14(a)]. For a point source and a curved monochromator crystal, one specific curvature can compensate for this variation in incidence angle [Fig. 14(b)]. The reflected spectral bandwidth is then at a minimum; this setting is known as the ‘Guinier position’. If the curvature of the monochromator crystal is increased further, a range of photon wavelengths,  $(\delta\lambda/\lambda)_{\text{corr}}$ , is selected along its length so that the rays converging towards the focus have a correlation of photon wavelength and direction [Fig. 14(c)]. This is used in

dispersive measurements, *e.g.* see Arndt *et al.* (1982) and Renevier *et al.* (2003). The effect of a finite source is to cause a change in incidence angle at the monochromator crystal, so that at the focus there is a photon-wavelength gradient across the width of the focus (for all curvatures) [Fig. 14(d)]. The use of a slit in the focal plane is akin to placing a slit at the tangent point to limit the source size.

The double-crystal monochromator with two parallel or nearly parallel perfect crystals of germanium or silicon is a common configuration. The advantage of this is that the outgoing monochromatic beam is parallel to the incoming beam, although it is slightly displaced vertically by an amount  $2d \cos \theta$ , where  $d$  is the perpendicular distance between the crystals and  $\theta$  the monochromator Bragg angle. The monochromator can be rapidly tuned, since the diffractometer or camera need not be re-aligned significantly in a scan across an absorption edge. Between absorption edges, some vertical adjustment of the diffractometer is required. Since the rocking width of the fundamental is broader than the harmonic reflections, the strict parallelism of the pair of crystal planes can be relaxed, *i.e.* detuned so that the harmonic can be rejected with little loss of the fundamental intensity. The spectral spread in the reflected monochromatic beam is determined by the source divergence accepted by the monochromator, the angular size of the source and the monochromator rocking width (see Fig. 15).

The double-crystal monochromator is often used with a toroid focusing mirror; the functions of monochromatization are then separated from the focusing (Hastings *et al.*, 1978).

The rocking width of a reflection depends on the horizontal and vertical beam divergences/convergences (after due account for collimation is taken)  $\gamma_H$  and  $\gamma_V$ , the spectral spreads  $(\delta\lambda/\lambda)_{\text{conv}}$  and  $(\delta\lambda/\lambda)_{\text{corr}}$ , and the mosaic spread  $\eta$ . We assume that  $\eta \gg \omega$ , where  $\omega$  is the angular broadening of a *relp* due to a finite sample. In the case of synchrotron radiation,  $\gamma_H$  and  $\gamma_V$  are usually widely asymmetric. On a conventional source, usually  $\gamma_H \simeq \gamma_V$ .

Two types of spectral spread occur with synchrotron and neutron sources (Greenough & Helliwell, 1982; Schoenborn, 1983). The term  $(\delta\lambda/\lambda)_{\text{conv}}$  is the spread that is passed down each incident ray in a divergent or convergent incident beam; the subscript refers to conventional source type. This is because it is similar to the  $K\alpha_1$ ,  $K\alpha_2$  line widths and separa-

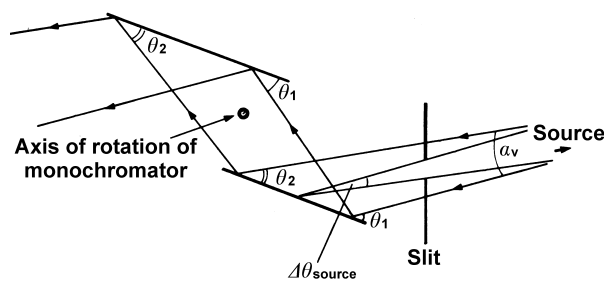


**Figure 15** Double-crystal monochromator illuminated by synchrotron radiation. The contributions of the source divergence  $\alpha_v$  and angular source size  $\Delta\theta_{\text{source}}$  to the range of energies reflected by the monochromator are shown.

tion. At the synchrotron, this component also exists and arises from the monochromator rocking width and finite-source-size effects. The term  $(\delta\lambda/\lambda)_{\text{corr}}$  is special to the synchrotron or neutron case. The subscript ‘corr’ refers to the fact that the ray direction can be correlated with the photon or neutron wavelength. Usually, an instrument is set to have  $(\delta\lambda/\lambda)_{\text{corr}} = 0$ . In the most general case, for a  $(\delta\lambda/\lambda)_{\text{corr}}$  arising from the horizontal ray direction correlation with photon energy, and the case of a horizontal rotation axis, then the rocking width  $\varphi_{\text{R}}$  of an individual reflection is given by

$$\varphi_{\text{R}} = \left\{ L^2 \left[ \left( \frac{\delta\lambda}{\lambda} \right)_{\text{corr}}^2 d^{*2} + \zeta\gamma_{\text{H}} \right]^2 + \gamma_{\text{V}}^2 \right\}^{1/2} + 2\varepsilon_{\text{s}}, \quad (71)$$

where

$$\varepsilon_{\text{s}} = \frac{d^* \cos \theta}{2} \left[ \eta + \left( \frac{\delta\lambda}{\lambda} \right)_{\text{conv}} \tan \theta \right] \quad (72)$$

and  $L$  is the Lorentz factor  $1/(\sin^2 2\theta - \zeta^2)^{1/2}$ .

The Guinier setting of the instrument gives  $(\delta\lambda/\lambda)_{\text{corr}} = 0$ . The equation for  $\varphi_{\text{R}}$  then reduces to

$$\varphi_{\text{R}} = L[(\zeta^2\gamma_{\text{H}}^2 + \gamma_{\text{V}}^2/L^2)^{1/2} + 2\varepsilon_{\text{s}}] \quad (73)$$

(from Greenhough & Helliwell, 1982). For example, for  $\zeta = 0$ ,  $\gamma_{\text{V}} = 0.2$  mrad ( $0.01^\circ$ ),  $\theta = 15^\circ$ ,  $(\delta\lambda/\lambda)_{\text{conv}} = 1 \times 10^{-3}$  and  $\eta = 0.8$  mrad ( $0.05^\circ$ ), then  $\varphi_{\text{R}} = 0.08^\circ$ . But  $\varphi_{\text{R}}$  increases as  $\zeta$  increases [see Greenhough & Helliwell (1982, Table 5)].

In the rotation/oscillation method as applied to protein and virus crystals, a small angular range is used per exposure

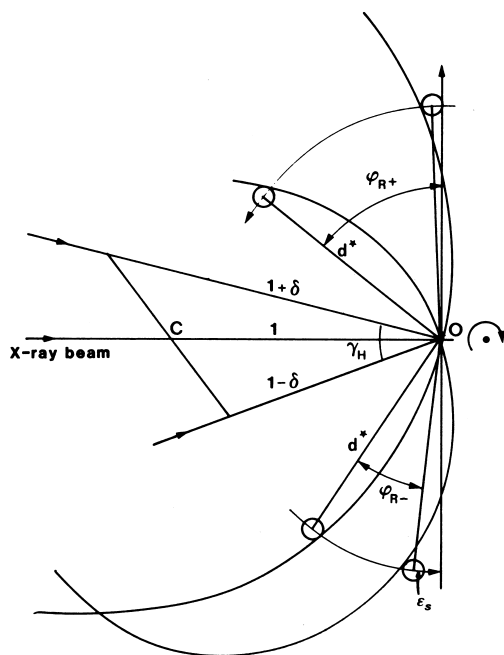


**Figure 16**

The rocking width of an individual reflection for the case of Fig. 14(c) and a vertical rotation axis.  $\varphi_{\text{R}}$  is determined by the passage of a spherical volume of radius  $\varepsilon_{\text{s}}$  (determined by sample mosaicity and a conventional-source-type spectral spread) through a nest of Ewald spheres of radii set by  $\delta = \frac{1}{2}[(\delta\lambda/\lambda)_{\text{corr}}]$  and the horizontal convergence angle  $\gamma_{\text{H}}$ . From Greenhough & Helliwell (1982).

(Section 3.4). For example,  $\Delta\varphi_{\text{max}}$  may be  $1.5^\circ$  for a protein, and  $0.4^\circ$  or so for a virus. Many reflections will be only partially stimulated over the exposure. It is important, especially in the virus case, to predict the degree of penetration of the relp through the Ewald sphere. This is done by analysing the interaction of a spherical volume for a given relp with the Ewald sphere. The radius of this volume is given by

$$E \simeq \frac{\varphi_{\text{R}}}{2L} \quad (74)$$

(Greenhough & Helliwell, 1982). For discussions, see Harrison *et al.* (1985) and Rossmann (1985).

In Fig. 16, the relevant parameters are shown. The diagram shows  $(\delta\lambda/\lambda)_{\text{corr}} = 2\delta$  in a plane, usually horizontal, with a perpendicular (vertical) rotation axis, whereas the formula for  $\varphi_{\text{R}}$  above is for a horizontal axis. This is purely for didactic reasons since the interrelationship of the components is then much clearer. For full details, see Greenhough & Helliwell (1982).

(c) *The use of the X-ray laser to record ‘still’ diffraction images from micro- and nano-sized crystal samples.* Accurate modelling of the diffraction underpins the huge success of protein crystallography, using sophisticated models developed over many years. The properties of a synchrotron X-ray source monochromated beam were studied in great detail through numerous commissioning experiments with test samples (Helliwell *et al.*, 1982). A similar strategy was undertaken for the characterization of a ‘white’ X-ray beam with and without beam-conditioning elements (reflecting mirrors and filters). However, the X-ray laser as a new source poses new challenges for detailed characterization owing to its stochastic nature. The ultra-intense nature of the X-ray beam, whilst being formed of ultra-short time pulses, allows ‘only’ a single diffraction pattern to be collected as there is no time to rotate the crystal sample. Finally, the smallest crystal samples now studied (in the nanometre size range) for structures with quite large unit cells leads to relatively few unit cells being irradiated and thereby the ‘grating interference function’ is broadened. The use of many individual single-crystal X-ray diffraction patterns representing many orientations can make a merged single X-ray diffraction data set of good data completeness. In many studies of this kind a Monte Carlo approach to merging the still diffraction patterns (‘stills’) was used; typically many hundreds of thousands of these stills made up one data set. Attempts to refine the partiality of each measured diffraction spot have gradually been made, to good effect in terms of greatly reducing the number of nanocrystals used. For a description of the progress the reader is referred to the overview of Sauter (2015).

Whilst this section has focused on micrometre- and nanometre-sized crystals studied one by one by serial crystallography, a method initiated at XFELs, the use of a large single crystal is also possible. This allows many X-ray diffraction shots across the crystal, which is displaced and rotated between the XFEL shots, to be measured (Ago, 2014).

## 7.4. Geometric effects and distortions associated with area detectors

Electronic area detectors are real-time image-digitizing devices under computer control. The mechanism by which an X-ray photon is captured is different in the various devices available (*i.e.* gas chambers, television detectors, charge-coupled devices, pixel detectors) and is different specifically from film or image plates. Arndt (1986) has reviewed the various devices available, their properties and performances [see also Sections 7.1.6 and 7.1.8 of the previous edition of *International Tables for Crystallography*, Vol. C (2006); Section 7.1.8 deals with storage phosphors, image plates and pixel detectors]. Fourme (1997) provides an update on position-sensitive gas detectors.

(a) *Obliquity*. In terms of the geometric reproduction of a diffraction-spot position, size and shape, photographic film gives a virtually true image of the actual diffraction spot. This is because the emulsion is very thin and, even in the case of double-emulsion film, the thickness,  $g$ , is only  $\sim 0.2$  mm. Hence, even for a diffracted ray inclined at  $2\theta = 45^\circ$  to the normal to the film plane, the ‘parallax effect’,  $g \tan 2\theta$ , is very small (see below for details of when this is serious). With film, the spot size is increased owing to oblique or non-normal incidence. The obliquity effect causes a beam, of width  $w$ , to be recorded as a spot of width

$$w' = w \sec 2\theta. \quad (75)$$

For example, if  $w = 0.5$  mm and  $2\theta = 45^\circ$ , then  $w'$  is 0.7 mm. With an electronic area detector, obliquity effects are also present. In addition, the effects of parallax, point-spread factor and spatial distortions have to be considered.

(b) *Parallax*. In the case of a one-atmosphere xenon-gas chamber of thickness  $g = 10$  mm, the  $g \tan 2\theta$  parallax effect is dramatic [see Hamlin (1985, p. 435)]. The wavelength of the beam has to be considered. If a  $\lambda$  of  $\sim 1$  Å is used with such a chamber, the photons have a significant probability of fully traversing such a gap and parallax will be at its worst; the spot is elongated and the spot centre will be different from that predicted from the geometric centre of the diffracted beam. If a  $\lambda$  of 1.54 Å is used then the penetration depth is reduced and an effective  $g$ , *i.e.*  $g_{\text{eff}}$ , of  $\sim 3$  mm would be appropriate. The use of higher pressure in a chamber increases the photon-capture probability, thus reducing  $g_{\text{eff}}$  *pro rata*; at four atmospheres and  $\lambda = 1.54$  Å, parallax is very small.

In general, we can take account of obliquity and parallax effects whereby the measured spot width, in the radial direction, is  $w''$ , where

$$w'' = w \sec 2\theta + g_{\text{eff}} \tan 2\theta. \quad (76)$$

As well as changing the spot size, the spot position, *i.e.* its centre, is also changed by both obliquity and parallax effects by  $\frac{1}{2}(w'' - w)$ . The spherical drift-chamber design eliminated the effects of parallax (Charpak *et al.*, 1977). In the case of a phosphor-based television system, the X-rays are converted into visible light in a thin phosphor layer so that parallax is negligible.

(c) *Point-spread factor*. Even at normal incidence, there will be some spreading of the beam size. This is referred to as the point-spread factor, *i.e.* a single pencil ray of light results in a finite-sized spot. In the TV-detector, CCD-with-phosphor and image-plate cases, the graininess of the phosphor and the system imaging the visible light contribute to the point-spread factor. In the case of a CCD used in direct-detection mode, *i.e.* X-rays impinging directly on the silicon chip, the point-spread factor is negligible for a spot of typical size.

(d) *Spatial distortions*. The spot position is affected by spatial distortions. These non-linear distortions of the predicted diffraction spot positions have to be calibrated for independently; in the worst situations, misindexing would occur if no account were taken of these effects. Calibration involves placing a geometric plate, containing a perfect array of holes, over the detector. The plate is illuminated, for example, with radiation from a radioactive source or scattered from an amorphous material at the sample position. The measured positions of each of the resulting ‘spots’ in detector space (units of pixels) can be related directly to the expected position (in mm). A 2D, non-linear, pixel-to-mm and mm-to-pixel correction curve or look-up table is thus established.

These are the special *geometric* effects associated with detectors. We have not discussed non-uniformity of response of detectors since this does not affect the geometry. Calibration for non-uniformity of response is discussed in Section 7.1.6 of the previous edition of *International Tables for Crystallography*, Vol. C (2006).

## 8. FAIR data and core metadata

In the FAIR raw data era (where raw data are described as, or not, Findable, Accessible, Interoperable and Reusable), the opportunity exists to archive the raw diffraction data as digital storage has expanded enormously. In the reprocessability of the raw data the geometric position of the beam centre must be part of the recorded metadata. Full details, and other core metadata relevant to this chapter, are given in the IUCr’s Diffraction Data Deposition Working Group Final Report 2017 (<https://www.iucr.org/resources/data/dddwg/final-report>).

## Acknowledgements

I am very grateful to various colleagues at the Universities of York and Manchester for their comments on the text of the first edition. However, special thanks go to Dr T. Higashi who commented extensively on the manuscript and found several errors. Any remaining errors are, of course, my own responsibility. Dr F. C. Korber is thanked for his comments on the diffractometry section. Dr W. Parrish and Professor E. J. Dodson are also thanked for discussions. Mrs Y. C. Cook is thanked for typing several versions of the manuscript and Mr A. B. Gebbie is thanked for drawing the diagrams. I am grateful to Miss Julie Holt for secretarial help in the production of the second edition. For the 3rd edition I thank the two anonymous referees for their reports.

## References

- Ago, H. (2014). *SACLA Research Frontiers 2014*, pp. 132–133. [http://www.springer.or.jp/pdf/en/res\\_fro/14/133\\_134.pdf](http://www.springer.or.jp/pdf/en/res_fro/14/133_134.pdf).
- Amorós, J. L., Buerger, M. J. & Amorós, M. C. (1975). *The Laue Method*. New York: Academic Press.
- Andrews, S. J., Hails, J. E., Harding, M. M. & Cruickshank, D. W. J. (1987). *Acta Cryst.* **A43**, 70–73.
- Arndt, U. W. (1986). *J. Appl. Cryst.* **19**, 145–163.
- Arndt, U. W., Greenhough, T. J., Helliwell, J. R., Howard, J. A. K., Rule, S. A. & Thompson, A. W. (1982). *Nature*, **298**, 835–838.
- Arndt, U. W. & Willis, B. T. M. (1966). *Single Crystal Diffractometry*. Cambridge University Press.
- Arndt, U. W. & Wonacott, A. J. (1977). *The Rotation Method in Crystallography*. Amsterdam: North-Holland.
- Artymiuk, P. & Phillips, D. C. (1985). *Methods Enzymol.* **114A**, 397–415.
- Arzt, S., Campbell, J. W., Harding, M. M., Hao, Q. & Helliwell, J. R. (1999). *J. Appl. Cryst.* **32**, 554–562.
- Aslanov, L. A., Fetisov, G. V. & Howard, J. A. K. (1998). *Crystallographic Instrumentation*. Oxford: IUCr/Oxford Science Publications.
- Bernal, J. D. (1927). *J. Sci. Instrum.* **4**, 273–284.
- Bijvoet, J. M., Burgers, W. G. & Hägg, G. (1969). *Early Papers on Diffraction of X-rays by Crystals*, Vol. I. Dordrecht: Kluwer Academic Publishers.
- Bijvoet, J. M., Burgers, W. G. & Hägg, G. (1972). *Early Papers on Diffraction of X-rays by Crystals*, Vol. II. Dordrecht: Kluwer Academic Publishers.
- Billinge, S. J. L. (2019). *International Tables for Crystallography*, Volume H, *Powder Diffraction*, pp. 649–672. Chichester: Wiley.
- Blakeley, M. P. (2009). *Crystallogr. Rev.* **15**, 157–218.
- Blundell, T. L. & Johnson, L. N. (1976). *Protein Crystallography*. New York: Academic Press.
- Bonse, U., Materlik, G. & Schröder, W. (1976). *J. Appl. Cryst.* **9**, 223–230.
- Bragg, W. H. (1928). *An Introduction to Crystal Structure Analysis*. London: Bell.
- Bragg, W. L. (1949). *The Crystalline State: A General Survey*, pp. 30–33. London: Bell.
- Broennimann, Ch., Eikenberry, E. F., Henrich, B., Horisberger, R., Huelsen, G., Pohl, E., Schmitt, B., Schulze-Briese, C., Suzuki, M., Tomizaki, T., Toyokawa, H. & Wagner, A. (2006). *J. Synchrotron Rad.* **13**, 120–130.
- Brooks, I. & Moffat, K. (1991). *J. Appl. Cryst.* **24**, 146–148.
- Buerger, M. J. (1942). *X-ray Crystallography*. New York: John Wiley.
- Buerger, M. J. (1964). *The Precession Method*. New York: John Wiley.
- Carr, P. D., Cruickshank, D. W. J. & Harding, M. M. (1992). *J. Appl. Cryst.* **25**, 294–308.
- Cassetta, A., Deacon, A., Emmerich, C., Habash, J., Helliwell, J. R., McSweeney, S., Snell, E., Thompson, A. W. & Weisgerber, S. (1993). *Proc. R. Soc. London Ser. A*, **442**, 177–192.
- Charpak, G., Demierre, C., Kahn, R., Santiard, J. C. & Sauli, F. (1977). *Nucl. Instrum. Methods*, **141**, 449–455.
- Coppens, P. (1992). *Synchrotron X-ray Crystallography*. London: Academic Press.
- Cruickshank, D. W. J. (1992). *Time-resolved macromolecular crystallography: introductory remarks and a little history*. In *Time-Resolved Macromolecular Crystallography*, edited by D. W. J. Cruickshank, J. R. Helliwell & L. N. Johnson. Oxford Science Publications.
- Cruickshank, D. W. J., Carr, P. D. & Harding, M. M. (1992). *J. Appl. Cryst.* **25**, 285–293.
- Cruickshank, D. W. J., Helliwell, J. R. & Moffat, K. (1987). *Acta Cryst.* **A43**, 656–674.
- Cruickshank, D. W. J., Helliwell, J. R. & Moffat, K. (1991). *Acta Cryst.* **A47**, 352–373.
- Dauter, Z. & Wilson, K. S. (2001). *International Tables for Crystallography*, Volume F, *Crystallography of Biological Macromolecules*, pp. 211–230. Chichester: Wiley.
- Drenth, J. (1994). *Principles of Protein Crystallography*. Berlin, Heidelberg: Springer Verlag.
- Einspahr, H., Suguna, K., Suddath, F. L., Ellis, G., Helliwell, J. R. & Papiz, M. Z. (1985). *Acta Cryst.* **B41**, 336–341.
- Evans, H. T. & Lonsdale, K. (1959). *International Tables for X-ray Crystallography*, Vol. II, p. 164. Birmingham: Kynoch Press.
- Forsyth, J. B., Lawrence, R. T. & Wilson, C. C. (1988). *Nucl. Instrum. Methods Phys. Res. A*, **273**, 741–747.
- Fourme, R. (1997). *Nucl. Instrum. Methods Phys. Res. A*, **392**, 1–11.
- Friedrich, W., Knipping, P. & von Laue, M. (1912). *Sitzungsber. K. Bayer. Akad. Wiss. Muenchen*, pp. 303–322.
- Gemmi, M., Mugnaioli, E., Gorelik, T. E., Kolb, U., Palatinus, L., Boullay, P., Hovmöller, S. & Abrahams, J. P. (2019). *ACS Central Sci.* **5**, 1315–1329.
- Georgieva, D. G., Jiang, L., Zandbergen, H. W., Nicolopoulos, S. & Abrahams, J. P. (2008). In *EMC 2008 14th European Microscopy Congress*, 1–5 September 2008, Aachen, Germany, edited by M. Luysberg, K. Tillmann & T. Weirich. Berlin, Heidelberg: Springer. [https://doi.org/10.1007/978-3-540-85156-1\\_380](https://doi.org/10.1007/978-3-540-85156-1_380).
- Glover, I. D., Harris, G. W., Helliwell, J. R. & Moss, D. S. (1991). *Acta Cryst.* **B47**, 960–968.
- Glusker, J. P. & Trueblood, K. N. (1971). *Crystal Structure Analysis*, pp. 35–47. Oxford University Press.
- Glusker, J. P. & Trueblood, K. N. (1985). *Crystal Structure Analysis*, 2nd ed., pp. 42–60. Oxford University Press.
- Greenhough, T. J. & Helliwell, J. R. (1982). *J. Appl. Cryst.* **15**, 493–508.
- Hamilton, W. C. (1974). *International Tables for X-ray Crystallography*, Vol. IV, pp. 273–284. Birmingham: Kynoch Press.
- Hamlin, R. (1985). *Methods Enzymol.* **114A**, 416–451.
- Hamlin, R., Cork, C., Howard, A., Nielsen, C., Vernon, W., Matthews, D. & Xuong, Ng. H. (1981). *J. Appl. Cryst.* **14**, 85–93.
- Harrison, S. C., Winkler, F. K., Schutt, C. E. & Durbin, R. (1985). *Methods Enzymol.* **114A**, 211–236.
- Hart, M. (1971). *Rep. Prog. Phys.* **34**, 435–490.
- Hastings, J. B. (1977). *J. Appl. Phys.* **48**, 1576–1584.
- Hastings, J. B., Kincaid, B. M. & Eisenberger, P. (1978). *Nucl. Instrum. Methods*, **152**, 167–171.
- Helliwell, J. R. (1984). *Rep. Prog. Phys.* **47**, 1403–1497.
- Helliwell, J. R. (1985). *J. Mol. Struct.* **130**, 63–91.
- Helliwell, J. R. (1992). *Macromolecular Crystallography with Synchrotron Radiation*. Cambridge University Press. [Also published in paperback, 2005.]
- Helliwell, J. R. (2005). *Acta Cryst.* **D61**, 793–798.
- Helliwell, J. R. (2021). *Int. Tables Crystallogr. C*. <https://doi.org/10.1107/S1574870720014184>.
- Helliwell, T. J., Greenhough, P., Carr, S. A., Rule, P. R., Moore, A. W., Thompson, A. W. & Worgan, J. S. (1982). *J. Phys. E: Sci. Instrum.* **15**, 1363–1372.
- Helliwell, J. R. & Wilkinson, C. (1994). *X-ray and neutron Laue diffraction*. In *Neutron and Synchrotron Radiation for Condensed Matter Studies: Applications to Soft Condensed Matter and Biology*, Vol. III, edited by J. Baruchel, J. L. Hodeau, M. S. Lehmann, J. R. Regnard & C. Schlenker. Berlin: Springer Verlag.
- Henry, N. F. M., Lipson, H. & Wooster, W. A. (1951). *The Interpretation of X-ray Diffraction Photographs*. London: Macmillan.
- Higashi, T. (1989). *J. Appl. Cryst.* **22**, 9–18.
- Higashi, T. (1990). *J. Appl. Cryst.* **23**, 253–257.
- Howard, A., Nielsen, C. & Xuong, Ng. H. (1985). *Methods Enzymol.* **114A**, 452–472.
- International Tables for Crystallography* (2006). Vol. C, *Mathematical, Physical and Chemical Tables*. Heidelberg: Springer.
- International Tables for X-ray Crystallography* (1959). Vol. II. Birmingham: Kynoch Press.
- Jeffery, J. W. (1958). *Z. Kristallogr.* **110**, 321–328.

- Kohra, K., Ando, M., Matsushita, T. & Hashizume, H. (1978). *Nucl. Instrum. Methods*, **152**, 161–166.
- Lairson, B. M. & Bilderback, D. H. (1982). *Nucl. Instrum. Methods Phys. Res.* **195**, 79–83.
- Langan, P., Greene, G. & Schoenborn, B. P. (2004). *J. Appl. Cryst.* **37**, 24–31.
- Lemonnier, M., Fourme, R., Rousseaux, F. & Kahn, R. (1978). *Nucl. Instrum. Methods*, **152**, 173–177.
- McKie, D. & McKie, C. (1986). *Essentials of Crystallography*. Oxford: Blackwell Scientific Publications.
- Messerschmidt, A. (2007). *X-ray Crystallography of Biomacromolecules: A Practical Guide*. Weinheim: Wiley-VCH.
- Moffat, K. (2001). *International Tables for Crystallography*, Volume F, *Crystallography of Biological Macromolecules*, pp. 205–210. Chichester: Wiley.
- Moffat, K., Schildkamp, W., Bilderback, D. H. & Volz, K. (1986). *Nucl. Instrum. Methods*, **A246**, 617–623.
- Nicolopoulos, S., Morniroli, J. P. & Gemmi, M. (2007). *Z. Kristallogr. Suppl.* **2007**, 183–188.
- Nieh, Y.-P. & Helliwell, J. R. (1995). *J. Synchrotron Rad.* **2**, 79–82.
- Nieh, Y. P., Raftery, J., Weisgerber, S., Habash, J., Schotte, F., Ursby, T., Wulff, M., Hädener, A., Campbell, J. W., Hao, Q. & Helliwell, J. R. (1999). *J. Synchrotron Rad.* **6**, 995–1006.
- Patterson, B. (2014). *Crystallogr. Rev.* **20**, 242–294.
- Rabinovich, D. & Lourie, B. (1987). *Acta Cryst.* **A43**, 774–780.
- Ren, Z., Bourgeois, D., Helliwell, J. R., Moffat, K., Šrajer, V. & Stoddard, B. L. (1999). *J. Synchrotron Rad.* **6**, 891–917.
- Renevier, H., Grenier, S., Arnaud, S., Bézar, J. F., Caillot, B., Hodeau, J. L., Letoublon, A., Proietti, M. G. & Ravel, B. (2003). *J. Synchrotron Rad.* **10**, 435–444.
- Rossmann, M. G. (1985). *Methods Enzymol.* **114A**, 237–280.
- Sakabe, N. (1983). *J. Appl. Cryst.* **16**, 542–547.
- Sakabe, N. (1991). *Nucl. Instrum. Methods Phys. Res. A*, **303**, 448–463.
- Sauter, N. K. (2015). *J. Synchrotron Rad.* **22**, 239–248.
- Schoenborn, B. P. (1983). *Acta Cryst.* **39**, 315–321.
- Schultz, A. J., Thiyagarajan, P., Hodges, J. P., Rehm, C., Myles, D. A. A., Langan, P. & Mesecar, A. D. (2005). *J. Appl. Cryst.* **38**, 964–974.
- Shmueli, U. (2007). *Theories and Techniques of Crystal Structure Determination*. Oxford: IUCr/Oxford Science Publications.
- Šrajer, V., Crosson, S., Schmidt, M., Key, J., Schotte, F., Anderson, S., Perman, B., Ren, Z., Teng, T., Bourgeois, D., Wulff, M. & Moffat, K. (2000). *J. Synchrotron Rad.* **7**, 236–244.
- Stout, G. H. & Jensen, L. H. (1968). *X-ray Structure Determination: a Practical Guide*, pp. 83–194. New York: Macmillan.
- Tanaka, I., Kusaka, K., Tomoyori, K., Niimura, N., Ohhara, T., Kurihara, K., Hosoya, T. & Ozeki, T. (2009). *Nucl. Instrum. Methods Phys. Res. A*, **600**, 161–163.
- Tickle, I. J., Sharff, A., Flensburg, C., Smart, O., Keller, P., Vornrhein, C., Paciorek, W. & Bricogne, G. (2021). STARANISO/PDBpeep Anisotropy Server. <https://staraniso.globalphasing.org/cgi-bin/PDBpeep.cgi>.
- Vainshtein, B. K. (1981). *Modern Crystallography*, Vol. I, pp. 297–300. Berlin: Springer.
- Vincent, R. & Midgley, P. A. (1994). *Ultramicroscopy*, **53**, 271–282.
- Wall, M. E. (1996). PhD Thesis, Princeton University. <http://public.lanl.gov/mewall/Wall-Princeton-1996.pdf>.
- Weisgerber, S. & Helliwell, J. R. (1993). *Faraday Trans.* **89**, 2667–2675.
- Weissenberg, K. (1924). *Z. Phys.* **23**, 229–238.
- Welberry, T. R. & Weber, T. (2016). *Crystallogr. Rev.* **22**, 2–78.
- Witz, J. (1969). *Acta Cryst.* **A25**, 30–42.
- Wlodawer, A. (1985). *Methods Enzymol.* **114A**, 551–564.
- Woolfson, M. M. (1970). *Introduction to X-ray Crystallography*. Cambridge University Press.
- Woolfson, M. M. (1997). *Introduction to X-ray Crystallography*, 2nd ed. Cambridge University Press.
- Wyckoff, H. W. (1985). *Methods Enzymol.* **114A**, 330–385.
- Wyckoff, H. W., Hirs, C. H. W. & Timasheff, S. N. (1985). *Methods Enzymol.* **114A**, 199–588.
- Xuong, N. H., Nielsen, C., Hamlin, R. & Anderson, D. (1985). *J. Appl. Cryst.* **18**, 342–350.